

**Development of Machine Learning-Based Metal Artefacts
Reduction Technique Using Multi-Energy Computed
Tomography**



By

Osama Sikander Khan

(Registration No: 00000326908)

Department of Biomedical Sciences

School of Mechanical and Manufacturing Engineering

National University of Sciences & Technology (NUST)

Islamabad, Pakistan

(2024)

**Development of Machine Learning-Based Metal Artefacts
Reduction Technique Using Multi-Energy Computed
Tomography**



By

Osama Sikander Khan

(Registration No: 00000326908)

A thesis submitted to the National University of Sciences and Technology, Islamabad,

in partial fulfillment of the requirements for the degree of

Master of Science in
Biomedical Sciences

Supervisor: Dr. Amer Sohail Kashif

Co Supervisor: Dr. Aamir Younis Raja


School of Mechanical and Manufacturing Engineering
National University of Sciences & Technology (NUST)

Islamabad, Pakistan

(2024)

THESIS ACCEPTANCE CERTIFICATE

Certified that final copy of MS/MPhil thesis written by **Regn No. 00000326908 Osama sikander Khan** of **School of Mechanical & Manufacturing Engineering (SMME)** has been vetted by undersigned, found complete in all respects as per NUST Statues/Regulations, is free of plagiarism, errors, and mistakes and is accepted as partial fulfillment for award of MS/MPhil degree. It is further certified that necessary amendments as pointed out by GEC members of the scholar have also been incorporated in the said thesis titled. **Development of machine learning-based metal artefacts reduction technique using multi-energy Computed Tomography.**

Signature: 

Name (Supervisor): Amer Sohail Kashif

Date: 04 - Apr - 2024

Signature (HOD): 

Date: 04 - Apr - 2024

Signature (DEAN): 

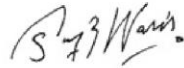


Date: 04 - Apr - 2024




National University of Sciences & Technology (NUST)
MASTER'S THESIS WORK

We hereby recommend that the dissertation prepared under our supervision by: Osama sikander Khan (00000326908)
Titled: Development of machine learning-based metal artefacts reduction technique using multi-energy Computed Tomography. be accepted in partial fulfillment of the requirements for the award of MS in Biomedical Sciences degree.

Examination Committee Members

1. Name: Muhammad Asim Waris Signature: 
2. Name: Muhammad Nabeel Anwar Signature: 
3. Name: Amer Sohail Kashif Signature: 

Supervisor: Amer Sohail Kashif

Signature: 

Date: 04 - Apr - 2024

04 - Apr - 2024


Head of Department

Date

COUNTERSIGNED

04 - Apr - 2024



Date

Dean/Principal

CERTIFICATE OF APPROVAL

This is to certify that the research work presented in this thesis, entitled “Development of Machine Learning-Based Metal Artefacts Reduction Technique Using Multi-Energy Computed Tomography” was conducted by Mr. Osama Sikander Khan under the supervision of Dr. Amer Sohail Kashif

No part of this thesis has been submitted anywhere else for any other degree. This thesis is submitted to the School of Mechanical and Manufacturing Engineering in partial fulfillment of the requirements for the degree of Master of Science in Field of Biomedical Sciences

Department of Biomedical Sciences National University of Sciences and Technology, Islamabad.

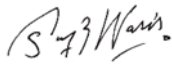
Student Name: Osama Sikander Khan

Signature:  _____

Supervisor Name: Amer Sohail Kashif

Signature:  _____

Name of Dean/HOD: Muhammad Asim Waris

Signature:  _____

AUTHOR'S DECLARATION

I, Osama Sikander Khan, hereby state that my MS thesis titled “Development of Machine Learning-Based Metal Artefacts Reduction Technique Using Multi-Energy Computed Tomography” is my own work and has not been submitted previously by me for taking any degree from National University of Sciences and Technology, Islamabad or anywhere else in the country/ world.

At any time if my statement is found to be incorrect even after I graduate, the university has the right to withdraw my MS degree.

Name of Student: Osama Sikander Khan

Date: 4th April 2024

PLAGIARISM UNDERTAKING

I solemnly declare that research work presented in the thesis titled “**Development of Machine Learning-Based Metal Artefacts Reduction Technique Using Multi-Energy Computed Tomography**” is solely my research work with no significant contribution from any other person. Small contribution/ help wherever taken has been duly acknowledged and that complete thesis has been written by me.

I understand the zero tolerance policy of the HEC and National University of Sciences and Technology (NUST), Islamabad towards plagiarism. Therefore, I as an author of the above titled thesis declare that no portion of my thesis has been plagiarized and any material used as reference is properly referred/cited.

I undertake that if I am found guilty of any formal plagiarism in the above titled thesis even after award of MS degree, the University reserves the rights to withdraw/revoke my MS degree and that HEC and NUST, Islamabad has the right to publish my name on the HEC/University website on which names of students are placed who submitted plagiarized thesis.

Student Signature:  _____

Name: Osama Sikander Khan

Dedicated to my exceptional parents, beloved wife, cherished siblings, and supportive friends whose unwavering encouragement and collaboration have been instrumental in achieving this significant milestone.

ACKNOWLEDGEMENTS

I am thankful to my Creator Allah Subhana-Watala to have guided me throughout this work at every step and for every new thought which He setup in my mind to improve it. Indeed I could have done nothing without His priceless help and guidance. Whosoever helped me throughout the course of my thesis, whether my parents or any other individual was His will, so indeed none be worthy of praise but Him.

I am profusely thankful to my beloved parents who raised me when I was not capable of walking and continued to support me throughout in every department of my life.

I would also like to express special thanks to my supervisor Dr. Amer Kashif for her help throughout my thesis. I would also to thank my Co-Supervisor Dr. Aamir Younis Raja, without whom this project wouldn't have been possible. He helped me not only in understanding the problem but also guided me towards the solution every step of the way.

I would also like to pay special thanks to my wife Laiba Hareem Raza for her tremendous support and cooperation. She supported me every step of the way and pushed me to do better and aim higher. Without her help I wouldn't have been able to complete my thesis.

I would also like to thank Urooba Tariq, Nimra Idrees, Sahar Fatima, Amna Idrees, Jannat Imran for being my thesis guidance and express my special thanks to for their help.

Finally, I would like to express my gratitude to all the individuals who have rendered valuable assistance to my study.

TABLE OF CONTENTS

| | |
|---|-------------|
| ACKNOWLEDGEMENTS | VIII |
| TABLE OF CONTENTS | IX |
| LIST OF TABLES | XI |
| LIST OF FIGURES | XII |
| LIST OF SYMBOLS, ABBREVIATIONS AND ACRONYMS | XIII |
| ABSTRACT | XIV |
| CHAPTER 1: INTRODUCTION | 1 |
| 1.1 Physical Principles of Photon-Counting CT | 4 |
| 1.2 Benefits of Photon-counting CT | 4 |
| 1.3 Problems with Photon-counting CT | 6 |
| 1.4 Effects of acquisition parameters | 8 |
| 1.5 Applications of Photon-counting CT: | 9 |
| 1.6 Metal Artefacts Reduction (MAR) Algorithms | 11 |
| CHAPTER 2: LITERATURE REVIEW | 15 |
| 2.1 Conventional MAR Approaches: | 15 |
| 2.1.1 Projection Domain: | 15 |
| 2.1.2 Image domain | 17 |
| 2.1.3 Iterative reconstruction | 21 |
| 2.2 Deep Learning Based MAR: | 23 |
| CHAPTER 3: METHODOLOGY | 27 |
| 3.1 MARS Microlab 5x120 | 27 |
| 3.2 Medipix 3RX Chip | 29 |
| 3.3 QRM Phantom | 30 |
| 3.4 Data Acquisition | 31 |

| | |
|---|-----------|
| 3.5 Artefact Free Simulation | 33 |
| 3.6 Deep Learning MAR Algorithm | 34 |
| 3.6.1 ResNet | 35 |
| 3.6.2 Densenet | 36 |
| 3.6.3 U-net | 36 |
| 3.6.4 RDU-Net (Proposed Method) | 36 |
| 3.7 Evaluation Strategy | 37 |
| 3.7.1 Energy Analysis | 37 |
| 3.7.2 Material Analysis | 39 |
| | |
| CHAPTER 4: RESULTS | 41 |
| 4.1 Energy Analysis: | 41 |
| 4.2 Material Analysis | 45 |
| | |
| DISCUSSION | 47 |
| | |
| CONCLUSION & FUTURRE PROSPECTS | 49 |
| | |
| REFERENCES | 50 |

LIST OF TABLES

| | Page No. |
|---|-----------------|
| Table 2.1: Conventional MAR approaches in the projection domain | 15 |
| Table 2.2: Conventional MAR approaches in the Image domain | 17 |
| Table 2.3: Conventional MAR approaches using iterative reconstruction | 22 |
| Table 2.4: Deep Learning-based MAR approaches | 23 |
| Table 4.1 Material Identification (sensitivity, specificity, Accuracy, NPV, and PPV) and quantification (RMSE) analysis | 46 |

LIST OF FIGURES

| | |
|---|----|
| Figure 3.1 Methodological pipeline implemented in this study | 27 |
| Figure 3.2 MARS Microlab 5x120 | 28 |
| Figure 3.3 QRM Phantom and all the available inserts | 31 |
| Figure 3.4 Illustration of different datasets used in this study | 33 |
| Figure 3.5 Architecture and functioning of the RDU-Net Model For MAR | 35 |
| Figure 4.1 Validation dataset | 41 |
| Figure 4.2 Line profiles..... | 42 |
| Figure 4.3 Histograms..... | 43 |
| Figure 4.4 Evaluation metrics for the MAR algorithm | 44 |
| Figure 4.5 Results of the Material Analysis after using MAR algorithm | 45 |

LIST OF SYMBOLS, ABBREVIATIONS AND ACRONYMS

| | |
|---------|-------------------------------------|
| CT | Computed Tomography |
| MAR | Metal Artefacts Reduction |
| PCCT | Photon-counting Computed Tomography |
| MD | Material Decomposition |
| RDU-Net | Residual Dense U-Net |

ABSTRACT

Computed Tomography (CT) is a commonly used diagnostic tool that uses X-Rays in order to detect and diagnose injuries, tumors and other diseases by providing an in-depth view inside the patient's body. A CT scanner takes cross sectional images of your body in layers or "slices". This technique helps diagnosticians to be able to observe the patient's body in great detail. However, one of the major problems in CT imaging is that of artifacts caused by high-density regions in the vicinity of normal tissues, for example calcified regions and metal implants. These high-density regions in the CT images could cause false voxel values. The study aimed to develop an innovative machine learning-based technique called residual dense U-Net (RDU-Net), specifically for spectral photon-counting CT (SPCCT), to mitigate metal artefacts across all energy bins. The proposed model was quantitatively evaluated and compared with and without the metal artefact reduction algorithm (MAR) using the line profiles, histogram analysis, signal-to-noise ratio (SNR), root mean squared error (RMSE), and structural similarity index measure (SSIM). The results show significant improvements with the average SNR across the five energy bins increasing from 3.37 to 17.40 after the application of the MAR algorithm. The average RMSE decreased from 0.016 to 0.001, and the average SSIM increased by 34.9%. The study also evaluated material density images of hydroxyapatite (HA) and iodine (I), with and without the MAR, using the receiver operating characteristic (ROC) paradigm. The results showed improved accuracy in the material identification for HA (86% to 91%) and I (84% to 93%) after MAR. Overall, the evaluation of the model showed promising results and the potential to significantly decrease the metal artefacts in all the parameters used in the energy analysis while preserving the attenuation profile of SPCCT images.

CHAPTER 1: INTRODUCTION

Computed Tomography commonly known as CT is one of the most widely used diagnostic tool (Esses et al., 2004; Mettler Jr et al., 2008). CT scanning refers to the technique in which we used slices of X-Rays images to form a comprehensive three-dimensional depiction of the human body (Coupal et al., 2014). In order to measure the intensity of incoming photons, CT scanners are comprised of an X-ray emitter and an X-ray detector positioned in direct opposition to each other. Similar to a traditional X-ray equipment, a CT scanner releases radiations that are permitted to enter the human body and are subsequently absorbed in different amounts (Willi, 2006). However, the CT scanner rotates the gantry, which houses the X-ray emitter and detector, in an arc-like motion to obtain a circular slice of the designated area in order to detect a circular slice of the body (Withers et al., 2021). The subject is moved laterally while this process is repeatedly performed. This produces a range of slices from which we can construct a full three-dimensional image. Furthermore, by calculating the energy of the photons reaching the detector, the variation in the absorbed amount of the X-ray waves by various bodily sections and organs produces a clear internal image of the body. Energy-integrating detectors (EIDs) are used in clinical CT scanners to identify the incoming photons. These EIDs are kept in batches of 900 in a row, arranged linearly apart by a thin septum. These housings, together referred to as detector banks, comprise what is often known as a detector. A semiconductor material used to create an EID responds to the strength of the incoming photon. The top layer of the semiconductor, referred to as the scintillator, absorbs the incoming photons and transforms them into visible light rays. A photodiode, which makes up the detector's second layer, detects light rays and produces an electrical signal whose strength is proportionate to the energy of the deposited rays. We then utilize this electric signal to calculate the incoming X-ray photons' intensity. The CT scanners employ the Hounsfield unit (HU) to calculate the intensities. The dimensionless unit known as HU is employed to provide a quantitative scale for characterizing radio density. The definition of HU is derived from the radiation absorbance or attenuation coefficients in a body's tissues (DenOtter & Schubert, 2023). As our output, the HU values enable us to obtain a distinct multifaceted grayscale image (Gücük & Üyetürk, 2014).

Since its inception in the beginning of the 1970s, CT scanning has grown to be a widely used diagnostic technique. A comprehensive three-dimensional image of the body is provided by CT scanning, which is very helpful in the detection of a number of ailments, including liver masses, cancer, and cardiovascular disorders (Nicol et al., 2019) (Wijesekera et al., 2010). It also helps in detection of internal bleeding, complex bone fractures as well as aid in planning of various treatments (Battista et al., 1980; Sripes & Yaparpalvi, 2012). Nevertheless, a significant disadvantage of CT scanning is the blooming artifacts that result from high density areas in the body. Because metal is typically the origin of this, it is also referred to as "metal artifacts" because of how much more common these are (De Man et al., 1998). The issue of metal artifacts is getting worse on an exponential scale as metal implants become more widespread. There is an urgent need to develop a way to lessen or eliminate this artifact since precise CT scans are essential for both disease detection and diagnosis. Mechanisms include beam hardening, dispersion, noise, and the non-linear partial volume (NLPV) effect are among the most frequent causes of metal artifacts

The evaluation of tissues encompassing metal structures, including intracranial coils, clips, stents, orthopedic or dental implants, fixation devices, and other metallic items, is greatly impacted by these artifacts (Arabi & Zaidi, 2021; Liao et al., 2019). This restriction makes it difficult to see structures, making it more difficult to identify early-stage problems including inflammation, infection, and malignancies, as well as to evaluate how well metal implants integrate with bone tissue. (Gjesteby et al., 2016).

When an incoming beam interacts with high Z materials, such as metals, it becomes "hardened," which is the principal cause of beam hardening in polychromatic x-ray beams. This phenomenon happens because certain materials absorb photons with low energies considerably more readily, raising the average energy of the beam. Because of the attenuation mostly caused by Compton Scattering in the high energy beam that is left behind, the hardening of the x-ray beam alters the beam's course. Defects in the photonic paths caused by beam hardening and scattering now affect the attenuation profile calculation during the scan. This effect is so strong in metal items that it causes streaks to

emerge and the introduction of cupping artifacts ultimately resulting in loss of data and incorrect spectral profiles (Boas et al., 2012; Hunter & McDavid, 2012).

The non-linear partial volume (NLPV) effect happens when a metal object's edge is partially positioned along a projection line. The computed attenuation coefficient varies as a result of this. This indicates that the intensity calculated within this region no longer follows a linear function, which leads to a mistake in the data projection. An error occurs during the reconstruction of the picture profile due to this irregularity in the projection domain. (Glover & Pelc, 1980).

Due to the fact that statistical noise becomes more pronounced when dealing with lower photon counts—that is, when the photon flux measured by the detector deviates from the standard Poisson Distribution—noise also played a significant role in the creation of metal artifacts (Hsieh, 2009). Furthermore, electronic noise also becomes more noticeable at low signal levels, which causes sporadic, thin streaks of light and dark to appear in the reconstructed image (Lee et al., 2021). The combined effect of these artifacts produces wildly divergent results, particularly when spectral attenuation profiles are involved. It can also lead to errors in subsequent tasks, like material decomposition, where the accuracy of the attenuation profile is crucial to achieving the best possible results.

But we are now able to acquire an increasing amount of information from CT imaging because to improvements in the area and the introduction of new and superior CT equipment, such as multi-photon-counting CT. This has opened the door for more creative solutions to these issues. These developments allow us to extract a more comprehensive and thorough spectral attenuation profile from CT scans, and they have created new opportunities for innovative research aimed at diagnosing and identifying an increasing number of disorders within the human body from a single complete scan. It is therefore becoming extremely vital to increase the accuracy of the attenuation profiles we obtain from our CT scanners by now only removing artefacts from the reconstructed images but by also adjusting and correcting the required attenuation values in the spectral profiles.

1.1 Physical Principles of Photon-Counting CT

Counting photons CT has the power to significantly change clinical CT. The mechanics of the novel energy-resolving x-ray detectors employed in photon-counting CT differ greatly from those of the conventional energy-integrating detectors. Photon-counting CT detectors are those that measure and count incoming photons. Instead of using a separate layer to convert x-rays into light, photon-counting detectors (PCDs) use a single wide layer consisting of a diode made from semiconductors to which high-voltage electricity is supplied. (Ballabriga et al., 2021). The semiconductor creates a cloud of charges that are both positive and negative traveling in opposite directions if it absorbs a single x-ray. The electrical pulse that the moving charges in the electrodes produce is recorded by an electronic readout circuit. PCDs convert each individual x-ray photon directly into an electric signal, as opposed to EIDs, which are currently used in CT and need to convert photons to visible light first. Each photon that enters the detector element causes an electrical pulse to be produced, the height of which is inversely related to the amount of energy absorbed. The detector's electronics system keeps track of how many pulses have heights greater than the predetermined threshold level. The detector can then compare each pulse to a set of threshold values in order to classify the arriving photons into an array of energy bins (typically two to eight) based on the amount of energy they have (Leng et al., 2019). Higher contrast-to-noise ratios, improved spatial resolution, and tailored spectrum imaging are the outcomes of using PCDs (Willeminck et al., 2018). In contrast to current CT technology, photon-counting CT can reduce radiation exposure, improve the reconstruction of images with higher resolution, alleviate beam-hardening artifacts, enhance the administration of contrast agents, and pave the way for novel and more precise non-invasive diagnostic approaches. (Wu et al., 2023).

1.2 Benefits of Photon-Counting CT

Photon-counting CT is different from conventional CT in several key ways and these differences offer unique benefits (Danielsson et al., 2021) (Flohr et al., 2020). Some of these benefits are:

- a. **Data acquisition:** Conventional CT acquires continuous data from an X-ray source, while photon-counting CT acquires discrete data from individual photons. This results in a different data acquisition process, which can provide improved image quality and increased accuracy.
- b. **Dynamic range:** Because of its constrained dynamic range, conventional CT can provide pictures with significant intensity differences and low contrast. Photon-counting CT can capture pictures with better contrast because of its significantly greater dynamical range.
- c. **Radiation dose:** Photon-counting CT can use lower radiation doses compared to conventional CT, as it can use a lower X-ray flux while still achieving high image quality. This is particularly important in medical imaging, where minimizing radiation exposure is critical.
- d. **Image processing:** Advanced techniques that cannot be applied to standard CT data can be used to process CT data with photon-counting. This may lead to enhanced precision, better image quality, and new quantitative data that may be utilized for treatment planning and diagnostics.
- e. **Material composition:** Photon-counting CT can provide information about the material composition of the objects being imaged, as different materials interact differently with X-rays. This information can be used to produce images with improved contrast and to quantify the properties of materials.
- f. **Improved time resolution:** Photon-counting CT has the ability to accurately time stamp individual photons, which can provide improved time resolution compared to other types of detectors. This is important in applications such as time-resolved spectroscopy and laser-induced fluorescence imaging.
- g. **Improved data processing:** Photon-counting CT provides a digital signal that can be processed and analyzed by a computer, which enables advanced data processing techniques, such as image reconstruction and image analysis algorithms, to be used for improved image quality and quantitative analysis.
- h. **Reduced imaging artifacts:** Through the reduction of imaging aberrations such as scatter, metal, and beam hardening, photon-counting CT can increase picture accuracy.

1.3 Problems with Photon-counting CT

Photon-counting CT (Computed Tomography) is a relatively new technology and, like any other new technology, it has some problems and limitations that need to be addressed. Some of the current problems and limitations of photon-counting CT include:

- a. **Cost:** Photon-counting CT systems are currently more expensive than conventional CT systems, which can limit their adoption and use in some clinical and research settings.
- b. **Complexity:** Photon-counting CT systems are more complex than conventional CT systems, which can make them more difficult to use and maintain. The data acquisition and processing systems for photon-counting CT are also more complex than those for conventional CT, which can increase the time and effort required to produce images.
- c. **Limited availability:** Photon-counting CT systems are currently not widely available, and they are only available at select research and medical institutions. This limits the ability of researchers and clinicians to use and test the technology, and it can also limit the availability of data and information about its benefits and limitations.
- d. **Data acquisition time:** Photon-counting CT systems typically require more time to acquire data than conventional CT systems, which can limit their use in clinical settings where speed is important.
- e. **Image quality:** Even though photon-counting CT has the ability to create high quality pictures with enhanced contrast, precision, and lower noise, other factors including noise, photon hunger, and artifacts from data processing can still affect the image quality.
- f. **Radiation dose:** Although photon-counting CT can use lower radiation doses compared to conventional CT, it still requires the use of ionizing radiation, which can be a concern for some patients and healthcare providers.
- g. **Image analysis:** The advanced data processing techniques used in photon-counting CT can also introduce new sources of error and artifacts into the images, which can limit the accuracy of the images produced and the results of the image analysis.

Moreover, the photon-counting detector that the PCT uses also comes with a lot of technical problems these that result in errors and noise in the images produced. Some of these technical challenges include:

- a. **Dead-Time:** Dead-time is the period during which a photon-counting detector is not able to detect incoming photons after a primary photon has been detected. This is caused by the time required for the detector to reset itself and prepare for the next photon. Dead time can result in errors in the measurement of the number of photons detected, and it can also result in photon starvation, where the number of photons detected is lower than the actual number of photons present.
- b. **Crosstalk:** Crosstalk occurs when two or more photons are counted as a single event, resulting in an overestimate of the number of photons detected. Crosstalk can result in image artifacts, such as streaking and blurring, and it can also result in an overestimate of the density of tissues in the image.
- c. **After-pulsing:** After-pulsing occurs when a detector counts an additional photon after a primary photon has been detected. This can result in errors in the measurement of the number of photons detected, and it can also result in image artifacts.
- d. **Nonlinearity:** Photon-counting detectors can have nonlinear response to incoming photons, which can result in errors in the measurement of the number of photons detected.
- e. **Dark Counts:** Dark counts are counts produced by the detector in the absence of incoming photons. These counts can result in errors in the measurement of the number of photons detected, and they can also result in noise in the images.
- f. **Pile-up:** Pile-up occurs when two or more photons arrive at the detector so closely in time that they are counted as a single event. Pile-up can result in errors in the measurement of the number of photons detected, and it can also result in image artifacts.
- g. **Data Processing Artifacts:** The data processing algorithms used to generate images from the data acquired by the photon-counting detector can also introduce errors and noise into the images. This can include errors introduced by the

correction of dead time and after-pulsing, as well as errors introduced by the image reconstruction algorithms.

To minimize these technical challenges, a number of methods have been developed, such as dead time correction algorithms, crosstalk correction algorithms, and image reconstruction algorithms that take into account the unique characteristics of photon-counting detectors. However, further research and development are needed to address these technical problems and to improve the performance of photon-counting detectors and photon-counting CT. And thus, while photon-counting CT has the potential to offer several benefits over conventional CT, such as improved image quality and radiation dose reduction, it also faces several technical challenges that result in errors and noise in the images produced. Addressing these technical challenges will be essential for the successful implementation and widespread adoption of photon-counting CT.

1.4 Effects of acquisition parameters

Adjusting the scanning parameters in photon-counting CT plays a major role in the reduction of artifacts and enhancement of the resultant images. Metal artifacts occur due to the interaction of X-rays with high-density materials like metal implants thus, changing acquisition parameters can greatly reduce these artifacts (Vellarackal & Kaim, 2021) (Richtsmeier et al., 2023) (Skornitzke et al., 2023) (Puvanasunthararajah et al., 2021). Acquisition parameters that can greatly affect these artefacts include:

- a. **Tube Voltage (kVp):** Changing the tube voltage affects the energy of the emitted X-ray photons. Increasing the tube voltage results in higher-energy photons which are less prone to being absorbed by the metal, reducing beam hardening artifacts caused by low-energy photons getting absorbed more readily.
- b. **Tube Current (mA):** Adjusting the tube current regulates the number of X-ray photons generated this in turn increases the signal-to-noise ratio, providing better images by reducing noise levels. However, this increases the radiation exposure to the patient and thus it is necessary to find a balance between image quality and dose.

- c. **Exposure Time:** Longer exposure times can potentially help capture more data, improving the image quality. However, longer exposure may also increase patient motion artifacts. Likewise, shorter exposure times may reduce motion artifacts but could lead to a decrease in image quality due to insufficient photon number of photons being detected.
- d. **Spectral Filtering:** Implementing spectral filters like tin filters can optimize the X-ray spectrum. These filters preferentially remove lower-energy photons, reducing the impact of beam hardening and scatter caused by metal implants.

In summary, tweaking acquisition parameters in photon-counting CT, such as tube voltage, current, exposure time and spectral filtering allows for customization to mitigate metal artifacts. However, these adjustments often involve trade-offs between image quality and radiation dose, necessitating careful optimization for especially in clinical scenarios.

1.5 Applications of Photon-counting CT:

Photon-counting CT has paved to various applications for medical imaging and diagnosis and has the ability to revolutionize the current healthcare system. Its ability to discriminate photon energies, advanced image reconstruction algorithms, and enhanced contrast-to-noise ratio contribute to its effectiveness across healthcare system. It can precisely analyse and utilize different energy levels and thus, PCCT can enhance diagnostic accuracy and provide a detailed anatomical and functional information which is critical for various medical disciplines.

Among these applications some of the most notable ones include:

- a. **Improved Soft Tissue Contrast:**

PCCT's has the capability to differentiate tissues based on their energy absorption profiles allowing for improved soft tissue contrast. This is achieved by analysing the varying attenuation characteristics of different tissues. PCCT acquires high-resolution images at multiple energy levels and therefore enhances the visualization of soft tissues. This is very crucial in oncology for detecting minute lesions, in

vascular imaging for precise delineation of vessels, and in neurological studies for accurate depiction of brain structures and pathologies.

b. Material Decomposition:

PCCT has energy-resolving capabilities which enables material differentiation by assessing how different materials interact with varying photon energies. It accurately identifies and distinguishes various materials, such as tissues, implants, or contrast agents, based on their unique energy absorption properties. Moreover, with new and improved algorithms PCCT is also able to perform material decompositions and is able to segment material profiles as well as quantify the amount of material present. This helps in identifying the location of various materials within the body, mitigating metal artifacts, and assessing the integration of implants into surrounding tissues.

c. Metal Artefacts Reduction:

Photon-counting CT effectively reduces the metal artifacts using multiple techniques. It utilizes energy thresholding to differentiate metal-related signals from imaging photons, using spectral analysis to identify the material composition and selectively exclude metal-induced artifacts. Advanced iterative reconstruction algorithms correct for metal impact on projections, reducing artifacts by compensating for scattering and beam hardening. Moreover, specific correction algorithms address photon starvation, scatter, and beam hardening caused by metal, enhancing image quality during reconstruction. Optimizing scanning parameters further aids in artifact reduction, balancing image quality with radiation exposure. These combined strategies enable photon-counting CT to produce clearer, diagnostically valuable images despite the presence of metal implants.

d. Low Radiation Dose Imaging:

PCCT has the ability to achieve high-quality images at lower radiation doses because of its efficient energy utilization and noise reduction capabilities. It uses photon-counting detectors to acquire high-resolution images while minimizing radiation exposure. This makes it particularly beneficial for paediatric imaging and scenarios where reducing radiation dose is especially important.

e. Quantitative Imaging and Material Analysis:

PCCT's photon-counting detector allow for quantitative assessment of tissue density and material composition. PCCT also provides precise measurements of tissue characteristics, such as bone density for osteoporosis evaluation and accurate material analysis for implants. By quantifying material composition, PCCT aids in understanding tissue properties and assessing health conditions more accurately.

f. Spectral Imaging and Functional Assessment:

The Spectral Imaging from PCCT allows for the assessment of tissue perfusion and function. PCCT can generate energy-specific images to map specific materials, such as iodine, aiding in angiography or organ perfusion studies. This provides insights into tissue functions and enhances the understanding of physiological processes.

g. Non-invasive Angiography and Cardiovascular Imaging:

PCCT enables high-resolution non-invasive imaging of blood vessels and cardiac structures and accurately delineates vascular structures, identifies plaque composition in coronary arteries, and assesses cardiovascular diseases. The technology's ability to provide detailed images with reduced artifacts means it can help with precise diagnoses in cardiac care.

h. Point-of-Care Imaging and Precision Medicine:

The enhanced image quality, portability, and reduced radiation exposure make PCCT very suitable for point-of-care imaging as well. It allows real-time diagnostics at the bedside, aiding in prompt decision-making and personalized patient care. Moreover, it's improved image quality and reduced artifacts facilitate accurate on-the-spot evaluations.

1.6 Metal Artefacts Reduction (MAR) Algorithms

Metal artifact reduction (MAR) is a crucial image processing technique used in computed tomography (CT) to mitigate the deleterious effects of metal artifacts on image quality and diagnostic accuracy. Metal artifacts commonly arise in CT imaging when highly attenuating materials, such as metal implants or foreign bodies, are present within the scanned region. These artifacts manifest as streaks, shadows, or bright spots in the

reconstructed CT images, leading to obscuration of anatomical structures, distortion of tissue boundaries, and degradation of image quality.

Metal Artefact Reduction (MAR) can be accomplished through the utilization of complex and sophisticated computational techniques, commonly referred to as MAR algorithms. MAR algorithms detect and segment the corrupted projection data caused by metallic implants, and further modify the corrupted data by replacing them with estimates of the corrected values. MAR techniques typically involve advanced image processing and reconstruction methods, often leveraging principles from signal processing, machine learning, and optimization theory. We can divide these algorithms into conventional and deep-learning-based approaches. Conventional methods typically involve mathematical models to identify and correct metal artifacts in CT images. These methods often rely on assumptions about the behavior of metal objects in the imaging process and employ strategies such as interpolation, segmentation, or statistical modeling to mitigate artifacts. While conventional algorithms have been widely used and have demonstrated effectiveness in certain scenarios, they may struggle to handle complex artifact patterns or variations in metal composition.

In contrast, deep-learning-based approaches leverage the power of artificial neural networks, particularly convolutional neural networks (CNNs), to automatically learn and extract complex features directly from the data. These algorithms are trained on large datasets of CT images with and without metal artifacts, allowing them to learn intricate mappings between corrupted and artifact-free images. Deep learning models excel at capturing subtle patterns and relationships in the data, making them well-suited for tasks like metal artifact reduction. By learning from data rather than relying on predefined rules or assumptions, deep-learning-based MAR algorithms can adapt to diverse artifact patterns and achieve superior performance in artifact suppression. However, they require large amounts of labeled training data and computational resources for training and inference. Nonetheless, their remarkable flexibility and effectiveness make them increasingly popular in the field of medical image reconstruction and artifact reduction.

MAR algorithms are categorized into four main groups

- Sinogram domain (Projection-Based)
- Image domain
- Dual Domain
- Iterative Approaches

a. Projection-Based MAR Algorithms:

These algorithms handle metal artifact reduction directly in the sinogram, which represents the raw data acquired by the CT scanner before image reconstruction. Projection-based methods focus mainly on identifying and rectifying corrupted data points caused by metals. Various techniques, such as forward projection, interpolation, or masking of corrupted projections, are employed to minimize the artifacts.

b. Image Domain MAR Algorithms:

Image domain approaches focus on correcting artifacts after the image has been reconstructed. The algorithms then identify metal regions within the reconstructed images. The algorithms then either correct the images in the image domain or forward-project these regions back into the sinogram where the corrupted projection data is replaced or corrected to reduce artifacts. Commercially available MAR algorithms often use this method due to its effectiveness in identifying and mitigating artifacts in the image domain.

c. Dual Domain MAR Algorithms:

Dual Domain methods, work simultaneously in both projection and image domain in order to achieve MAR. These methods leverage the strengths of each approach to overcome their respective limitations and achieve better artifact suppression in computed tomography (CT) images.

d. Iterative Approaches:

Iterative methods refine the CT images by repetitively updating and refining the reconstructed image. These approaches use mathematical optimization techniques, refining the image and gradually reducing the metal artefacts.

Each category aims to minimize metal artifacts by detecting, segmenting, and modifying the corrupted data caused by metal implants. They differ in the domain they primarily operate in – sinogram, reconstructed image, or through iterative image refinement. The selection of a specific approach often depends on the characteristics of artifacts present and the desired trade-offs between computational complexity and artifact reduction efficiency.

To summarize, photon-counting CT (PCCT) represents a significant advancement in medical imaging with potential to revolutionize the field of medical imaging. However, to completely utilize its benefits, thorough research is required to address the challenges associated with PCCT, particularly in mitigating metal artefacts. By minimizing these artefacts and preserving information, PCCT can be optimized for accurate diagnosis and comprehensive analysis, paving the way for its widespread clinical application and transformative impact on patient care.

CHAPTER 2: LITERATURE REVIEW

2.1 Conventional MAR Approaches:

2.1.1 Projection Domain:

This section details some of the conventional MAR approaches in the projection domain, where the metal artefacts are dealt with directly in the sinogram domain.

Table 2.1: Conventional MAR approaches in the projection domain

| Technique | CT type | Setup | Key feature |
|---|-----------------|--------------|---|
| Metal artifact reduction technique for flat detector based on forward projection (Prell et al., 2009) | FD-CT | Experimental | Increased CT value precision and reduced picture noise |
| Sinogram Total Variation (TV) inpainting (Duan et al., 2008) | Conventional CT | Simulation | <ul style="list-style-type: none"> • Images of superior quality after reconstruction • smoothly and accurately fill metal projection gaps |
| Iterative De-blurring for CT Metal Artifact Reduction (Wang et al., 1996) | Conventional CT | Simulation | <ul style="list-style-type: none"> • Simultaneous Iteration • Faster Convergence |
| Non-local Means Algorithm (Mouton et al., 2012) | Conventional CT | Experimental | Achieved notable gains over a reprojection-reconstruction method and a traditional linear interpolation-based approach. |

In (Prell et al., 2009), the forward projection-based metal artifact reduction (FP-MAR) and flat detector CT (FD-CT) correction algorithms that the authors have devised can suppress

secondary artifacts brought about by the interpolation approach and outperform 3DLI-MAR in all untruncated cases. It performs poorly on the, nevertheless. When the FOV is greater than the subject size, FP-MAR produces inferior results.

In (Duan et al., 2008) the authors have proposed Projection based MAR technique. The technique consists of TV painting method which consists of five steps, i.e. Initialization, segmentation, reprojection, inpainting and reconstruction respectively. Whereas setup and use FBP to recreate the image. Thresholding is used in segmentation to identify metal objects in the reconstructed image. The metal objects are reprojected to the Metal Projection Region (MPR) using reprojection. Metal items are inserted into the reconstructed inpainted data by the use of TV inpainting in MPR. The outcome demonstrates that in both noisy and noise-free incomplete projection data, TV inpainting performed better than linear interpolation. Nevertheless, this method's drawback is that it requires a high computing cost for handling spherical metal objects.

In (Wang et al., 1996) the authors have proposed an iterative method of the EM type, comparable to multi ART (MART). The primary distinction between the MART and EM iterative algorithms is the application of correction factors to the FOV after they have been concurrently computed while accounting for all projection profiles. The non-negativity restriction may have aided the EM-type reconstruction in achieving a faster convergence rate, according to the authors' additional comparison of the EM- along with ART-type iteration algorithms. However, the ART-type approach suppressed the noise better, maybe because the noise we added to the projection data was additive. The authors came to the conclusion that the computing complexity of the metal reduction using EM and ART types is the same.

This book-based method limits the intensity of the corrected pictures and uses the non-local means filters for post-filtering, which enhances the output of a traditional sinogram completion-based MAR strategy. The performance of the suggested method is assessed by the authors using both a conventional qualitative comparison according to visual quality and an entirely new quantitative analysis technique, which is based on the ratio of noisy 3D SIFT detection points found. Assessing the effect of MAR on the use of computer

vision algorithms for autonomous object identification is the primary goal of the quantitative analysis. According to the study, the suggested approach works better than algorithms based on reprojection-reconstruction and linear interpolation, especially when it comes to lowering the frequency of new artifacts in the fixed images. The positive results show that the suggested approach can enhance the effectiveness of computational and human evaluations of 3D CT baggage images for transportation security screenings. The suggested approach can aid in improving overall security measures and the detection of potentially harmful materials by lowering metal artifacts in 3D CT baggage images.

2.1.2 Image domain

This section details some of the conventional MAR approaches in the image domain, where the metal artefacts are dealt in the image domain after the reconstruction.

Table 2.2: Conventional MAR approaches in the Image domain

| Technique | CT Type | Data Acquisition Setup | Key Features |
|---|---------------------------------|-------------------------------|---|
| Novel subtraction method (S-MAR) (Zheng et al., 2022) | dual-layer detector spectral CT | Experimental | Subtracts out the contribution of metal artefacts and improves image quality |
| Constrained optimization (Zhang et al., 2011) | Fan-Beam CT | Simulated | Outperforms the FBP-type methods and ART and EM methods and yields artifacts-free images. |
| Tilted CT volume post-processing sets (Ballhausen et al., 2014) | Conventional CT | Experimental | <ul style="list-style-type: none"> • Computationally inexpensive • Comparable quantitatively to well-established techniques • Surpassing visually in a straight comparison |
| Techniques for Multi-Layer Entropic | Conventional CT | Experimental | Provides promising performance in detecting and removing metal artifacts from |

| | | | |
|--|-----------------|--------------|---|
| Thresholding and Label Filtering (Koonsanit et al., 2009) | | | dental CT images. |
| Additional Tilted Scan based CT (Kim et al., 2019) | Conventional CT | Both | Shows possibilities in identifying and eliminating metal artifacts from dental CT scans |
| Morphological image Filtering (Rodríguez-Gallo et al., 2019) | Conventional CT | Experimental | Significantly reduced artifacts and improve image quality. |
| Empirical Scatter Correction (ESC) (Meyer et al., 2010) | Conventional CT | Simulated | <ul style="list-style-type: none"> • Convenient and flexible method • Requires neither a precise calibration nor a great deal of prior knowledge. |

The article (Zheng et al., 2022) proposes a method that involves acquiring two CT scans of the same patient: one with the metal embolism coil in place and another without the coil. The two scans are then registered using a deformable registration algorithm, which aligns the two images based on their anatomical features. The aligned images are then subtracted, resulting in an image that shows only the tissue surrounding the metal coil, with reduced metal artifact. The authors name this approach as Novel subtraction method (S-MAR). The method was tested on 20 patients who had undergone cerebral aneurysm embolization using metal coils. The outcomes demonstrate a notable decrease in metal artifacts, improving the ability to see the surrounding tissue. In comparison to the uncorrected image, the suggested approach was able to minimize the metal artifact with an average of 51.3%.

In this article (Zhang et al., 2011), the authors present a constrained optimization-based approach that entails estimating the projection data that has been corrupted by metal artifacts and recovering the true attenuation coefficients through the use of a model that

makes use of background information about the imaging system and the object being imaged. The technique doesn't require any prior understanding of the precise geometry or substance of the implant because it is made to function with a variety of different metal implants. The constrained optimization method basically involves estimation of the corrupted projection data caused by metal artifacts using a forward projection model. Following this, the technique seeks to solve a limited optimization problem incorporating past information of the imaging system and the object being photographed in order to retrieve the true attenuation coefficients. When compared to the uncorrected photos, this method reduced the metal artifacts by up to 90%, and when compared with various state-of-the-art methods, it reduced them by up to 50%. Additionally, it showed a high level of precision and resilience with respect to various metal implant types and imaging systems, with no picture quality loss in non-metallic areas. However, the following method was found to be more time-consuming than some other methods, but can be improved with further optimization.

The authors in this method (Ballhausen et al., 2014) used a unique approach of acquiring a set of CT volumes that are tilted at different angles by using a tilting gantry that allows for the acquisition of tilted volumes. The tilted volumes are then reconstructed using standard CT reconstruction algorithms to produce a set of individual images, each with its own metal artifacts. Simple post-processing algorithm is used to correct the artifacts at first then the authors algorithm combines the tilted volumes into a final corrected using a combination of weighted averaging and interpolation of the voxel values in the individual images. Finally, an iterative refinement process is applied to the corrected volume to further reduce any residual metal artifacts. The algorithm was tested on a range of phantom and clinical datasets with metal implants, and compared with other state-of-the-art techniques for metal artifact reduction and was it reduced the metal artifacts by up to 75% compared to the uncorrected images.

In this study(Koonsanit et al., 2009), the authors propose a post-processing technique for automatically removing metal artifacts from dental CT scans, presuming that the artifact-containing pictures are already accessible. The suggested approach comprises of two steps: first, the dental region of the image is segmented using a regional entropy thresholding

methodology, and secondly, utilizing the connected pixel labeling concept, a label filtering technique is employed to remove isolated pixels, or the metal artifacts. Using hand-labeled dental pictures as the reference, this algorithm was tested on thirty sets of dental CT images, and its performance was assessed with regard to accuracy, sensitivity, and specificity. The algorithm's sensitivity was 87.89%, specificity was 99.54%, and accuracy was 99.21%, according to the results. These experiments demonstrated the robustness and effectiveness of the said method, which can notably improve the 3D visualization of CT images by automatically detecting and removing metal artifacts.

In this study(Kim et al., 2019), the researchers suggest a novel technique for minimizing metal artifacts in CT scans by utilizing complementing data from a separate slanted CT scan. The technique is based on the observation that the most noticeable metal artifacts in CT pictures are found along the direction of the x-ray beam, and that complementary information from an angled CT scan can be obtained without the presence of these metal abnormalities from the earlier scan. The procedure entails creating an image processing algorithm that suppresses the metal artifacts by using structural similarity (SSIM). Furthermore, if more suppression of metal artifacts in each scan is required, an established metal artifact reduction (MAR) technique can be applied. A simulation investigation of the pelvis region of an XCAT numerical phantom and a field test of the head area of the Rando phantom were used to validate the efficiency of the suggested method. The findings showed that, in both the simulation and experimental investigations, the suggested strategy successfully decreased the mean exact percentages of errors by as much as 86% and 89%, respectively.

In (Rodríguez-Gallo et al., 2019), the author proposes a morphological image filtering approach for MAR, called MIFMAR. In the MIFMAR algorithm, the metal implants are first identified in the CT-images using thresholding. Morphological picture filtering methods are then applied to the CT images to reduce the metal artifacts while preserving the surrounding tissues. The filtered images are then combined with the original CT images to produce final images with reduced metal artifacts and improved image quality. Three popular MAR techniques—linear interpolation (LI) as well as normalized metal artifact reduction (NMAR) and frequency split metal artifact reduction (FSMAR)—were

compared to MIFMAR. The linear-weighted κ test was utilized to assess inter-observer agreement, and the non-parametric Friedman-ANOVA test was employed to compare image quality across the various techniques. The outcomes demonstrate that, with good inter-observer acceptance, MIFMAR may effectively minimize metal artifacts in CT images while maintaining tissue features and enhancing image quality. In addition, there was a significant ($p < 0.01$) improvement in image quality & diagnostics scores when compared to the other three approaches. MIFMAR doesn't require raw CT data and is computationally cheap.

In this article (Meyer et al., 2010) the author proposes a fresh approach to CT scatter correction to get rid of metal artifacts in scans. Conventional scatter correction techniques rely on modeling the scatter content using scatter kernels based on raw data or data from Monte Carlo simulations of photon trajectories. These techniques take a lot of time and demand in-depth understanding of the spectral characteristics of the scanner. Here, they present an approach for empirical scatter correction (ESC) that doesn't require a lot of pre-knowledge or calibration. The ESC algorithm makes the assumption that a scatter-free linear combination that includes the uncorrected image and different ESC basis images exists. By optimizing a flatness condition of the combined volume, the coefficients comprising the linear combination are found in the image domain. By employing the gradient descent method in conjunction with a line search, the author reduced the overall variation in soft tissue regions. Then, with the addition of scatter using a Monte Carlo scatter calculation algorithm, they assessed ESC using both simulated data and multiple patient data sets obtained using a clinical cone-beam spiral CT scanner. These datasets also included metal implants simulations. Our initial findings show that ESC effectively minimizes metal artifacts as well as scatter artifacts in general. When compared to conventional techniques, ESC is more versatile, inexpensive to compute, and doesn't require knowledge of the parameters of the scanner.

2.1.3 Iterative reconstruction

This section details some of the conventional MAR approaches that remove metal artefacts using iterative reconstruction techniques.

Table 2.3: Conventional MAR approaches using iterative reconstruction

| Technique | CT Type | Data Acquisition Setup | Key Features |
|--|--------------------|-------------------------------|---|
| Constrained One-Step Spectral CT Image Reconstruction (cOSSCIR) (Schmidt et al., 2022) | Photon-counting CT | Simulated | By avoiding beam strengthening, noise, and photon hunger, cOSSCIR prevents metal artifacts. |

In this article (Schmidt et al., 2022) the author proposes the constrained one-step spectral CT image reconstruction (cOSSCIR) approach as a solution to metal artifacts in computed tomography (CT) that result from beam hardening, noise, and photon starvation. Using a physics-based forward model that takes beam hardening into account, the program directly calculates basis materials maps from photon-counting data. It then applies restrictions to the basis maps to stabilize the process of decomposition and lessen streaks brought on by noise and photon starvation. Because the spectral data is not required to be registered, the approach can be used even in cases when some energy window measures are not available. Photon-counting CT simulation of a virtualized pelvis phantom with symmetrical hip prosthesis and low-contrast soft tissue texture were used to test the algorithm. A "two-step" decomposition method and a non-spectral total variation restricted least-squares the reconstruction have been compared with the cOSSCIR images. With a standard variation of 20 HU in the central iodine region of interest and a quantitative error of -1 HU, the results demonstrated that cOSSCIR was more accurate and stable than the other approaches. Increasing photon deprivation did not change the cOSSCIR images' bias or standard deviation. The method reduced metal artifacts while accurately recreating the texture of soft tissue. All things considered, cOSSCIR offers a practical method for reducing metal artifacts in CT.

2.2 Deep Learning Based MAR:

This section details some of the prominent deep learning based MAR approaches that has shown reliable and accurate results.

Table 2.4: Deep Learning-based MAR approaches

| Technique | CT Type | Domain | Data Acquisition Setup | Key Features |
|---|--------------------|---------------|-------------------------------|---|
| Deep Residual Learning (Huang et al., 2018) | Conventional CT | Image | Simulated | Significantly lowers metal artifacts and enhances the view of important structures. |
| Self-supervised Cross-domain Learning (Yu et al., 2021) | Conventional CT | Image | Simulated | Yields better MAR results and performs better than other persuasive techniques. |
| Spectral Deep Learning (Busi et al., 2022) | Photon-counting CT | Image | Simulated | It is adaptable and generalizable to the current issue. |
| DoDoNet (Lin et al., 2019) | Conventional CT | Hybrid | Simulation | Radon consistency reduction, end-to-end dual domain network for MARCH, and radon inversion layer. |
| U-Net (Zhang & Yu, 2018) | Dental CT | Projection | Simulation | Reduced computational complexity |

| | | | | |
|-------------------------------------|---------------------|------------|------|--|
| CNN-MAR (Hegazy et al., 2019) | Convention al CT | Projection | Both | <ul style="list-style-type: none"> • RMSE decreases and the SSIM increases dramatically • performance depends upon the size of the training data |
|-------------------------------------|---------------------|------------|------|--|

To lessen metal artifacts within cervical CT images, the authors of (Huang et al., 2018) presented a unique residual learning technique that utilized a convolutional neural network (RL-ARCNN). For deep residual learning, the RL-ARCNN was trained on a dataset comprising artifact-free and artifact-residual images as well as artifact-inserted, to produce a large number of image patches. Then, using cervical CT scans, the model that had been trained was applied to MAR. On a test group of simulated artifact photos, the suggested approach produced a good MAR result with a peak signal-to-noise ratio (PSNR) of 38.09. The PSNR of residual learning has been determined to be greater than that of conventional learning, suggesting a notable reduction in artifacts with CNN-based residual imaging. In a 512x512 image, artifact removal took less than a second on avg. The investigators came at the conclusion that RL-ARCNN is a useful technique for lowering metal artifacts in cervical CT scans. It makes key structures easier to see and gives radiation oncologists more assurance when it comes to target delineation. This technique effectively removes metal artifacts without the need for sophisticated post-processing steps or sinogram data.

In (Yu et al., 2021) Lequan Yu suggests a deep learning-based method for metal artifact reduction (MAR). Based on a self-supervised cross-domain learning framework, his approach eliminates the need for pairs of CT scans with artifacts and those without, as it is a network learning technique. In the provided metal-free sinogram, where the metal trace is recognized by the forward projection of metallic masks, a neural network is trained to recover the values of the metal trace region. A newly developed filtered backprojection (FBP) reconstruction loss is applied to enhance the MAR image quality by motivating the network to produce more precise finishing results. Additionally, a residual-learning-based image refinement module is employed to lessen supplementary artifacts in the recreated CT images. The metal trace substitution is added to the overall framework and substitutes

the previous sinogram produced by the forward projection of the CNN output for the metal-affected projections of the original sinogram in order to maintain the fine structural features and authenticity of the final MAR picture. Lastly, he reconstructs the complete MAR image using FBP methods. The approach beats previous state-of-the-art approaches and yields superior MAR findings when tested on both simulated & real artifact data.

The method in (Busi et al., 2022) specifically uses the energy data from Spectral X-ray computed tomography (SCT). Although SCT reduces energy-dependent distortions, it still suffers from metal artifacts caused by photon starvation, especially in low-energy channels. The spectral deep learning-based metal artifact reduction technique has been presented to deal with this problem. The technique effectively minimizes streaked artifacts in all energy pathways and can improve low-energy reconstructive quality that has been impacted by metal artifacts. To enhance image quality, this method makes use of the extra data that is accessible in the energy domain. Additionally, the correction technique is parameter-free and takes only 15 ms per energy channel, which satisfies industrial scanners' need for near-real-time performance.

In order to address the issue of material artifacts, the authors of (Lin et al., 2019) have created a deep learning architecture known as an end-to-end trainable Dual Domain Network (DuDoNet), which simultaneously enhances CT images and restores the sinogram consistency. The Radon invert Layer, a Radon consistency loss, SE-Net, and IE-Net make up the model. The results of the experiments indicate that DuDoNET has outperformed the most advanced MAR approaches.

In The CNN-MAR model, an open artifact reduction framework that can separate tissue components from artifacts and merge the relevant data to create CNN images, was presented by the authors in (Zhang & Yu, 2018) The intended tissue manipulation technique is used to suppress the artifacts in order to produce a high-quality previous image. Statistical and clinical simulations have demonstrated that CNN-MAR can significantly minimize metal artifacts as well as restore fine features close to the metals.

In (Hegazy et al., 2019) the authors have introduced the U-NET model for the MAR in dental CT. The four distinct CT configurations—Unet-64, Unet-32, Unet-16, and Unet-8—

have been compared by the authors. According to the experiments, the computing speeds of U-net-32 and U-net-16 are boosted by approximately 3.6 and 7.3 times, respectively, when compared to U-net-64. Thus, with 7.3 times faster computing, U-net-16 was able to divide up the metallic regions with a degree of precision that was extremely close to that of the original U-net. The authors did, however, suggest that because of the small quantity of data the model is conditioned on, their technique is still unsuitable for clinical use.

In conclusion, there are a lot of MAR algorithms available, mostly for dual or conventional CT, but not many for PCCT. As a result, a MAR algorithm that is specifically made to correct multi-energy images obtained from SPCCT and that can operate simultaneously across multiple energy bins must be developed.

CHAPTER 3: METHODOLOGY

In this chapter, the details of the experimental procedures, data collection methods, and analytical techniques utilized to create our MAR algorithm. The overview of the methodology is described in a comprehensive workflow shown in Fig 3.1.

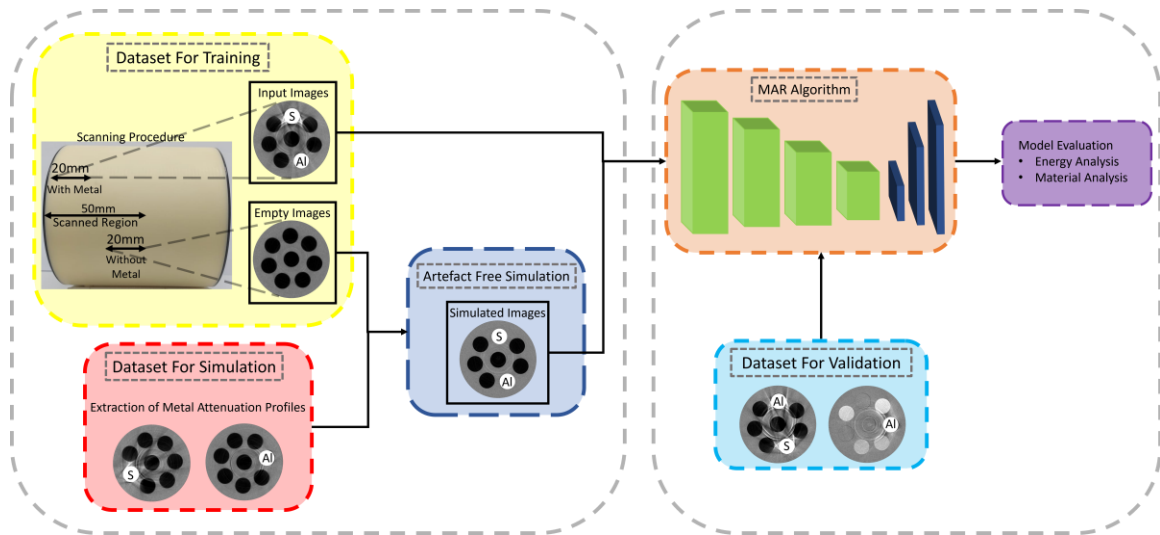


Figure 3.1 The figure presents the methodological pipeline implemented in this study. It shows the acquisition, processing, and utilization of datasets for the development and analysis of a machine learning-based Metal Artifact Reduction (MAR) algorithm.

3.1 MARS Microlab 5x120

The MARS Microlab 5x120 is a cutting-edge spectral photon-counting computed tomography (CT) scanner engineered by MARS Bioimaging Ltd. This advanced imaging system is designed to deliver high-resolution and energy-resolving imaging capabilities for various applications in medical diagnostics and research. At the heart of the MARS Microlab 5x120 lies its core technology, leveraging spectral photon-counting capabilities. It employs the Medipix 3RX chip, an innovative detector renowned for its ability to discern



Figure 3.2: Shows the MARS Microlab 5x120, a cutting-edge spectral photon-counting CT scanner engineered by MARS Bioimaging Ltd.

different energy levels of incoming photons. This chip is instrumental in achieving superior spectral resolution by dividing X-ray energy into discrete bins, allowing detailed analysis of different materials and tissues. The Medipix 3RX chip is a pivotal component within the scanner. It operates using charge summing mode and effectively segregates X-ray energy into five distinct energy bins. This functionality enables precise energy measurements, crucial for differentiating between various materials and tissues based on their energy absorption properties. The MARS Microlab 5x120 boasts high-resolution imaging capabilities, enabling detailed visualization of anatomical structures and materials. It offers exceptional spatial resolution, allowing for fine differentiation and analysis of tissues, materials, and artifacts. The scanner is equipped with customizable scan parameters, allowing meticulous control over imaging conditions. Operators can adjust tube current, tube voltage, slice thickness, number of projections, and energy thresholds to optimize image quality and capture specific energy ranges relevant to the study or diagnostic needs. This system empowers researchers and medical professionals with the means to delve into intricate material characterization and high-resolution diagnostics, contributing

significantly to advancements in both medical and scientific research domains (Moghiseh et al., 2023) (Ibrahim et al., 2024).

3.2 Medipix 3RX Chip

The Medipix 3RX chip stands as a pivotal component within photon-counting computed tomography (CT) systems, renowned for its remarkable capabilities in spectral imaging and precise energy resolution. Developed by CERN (European Organization for Nuclear Research), this chip constitutes a cornerstone of CT detectors, delivering advanced functionality that allows for enhanced differentiation of X-ray energies. It finds extensive application in medical imaging and material analysis due to its unparalleled features. Operating on the principle of direct conversion technology, the Medipix 3RX chip is ingeniously designed to interact with incoming X-ray photons. As X-rays penetrate the detector's semiconductor material—often silicon, Cadmium Telluride (CdTe), or Cadmium Zinc Telluride (CZT)—they create electron-hole pairs within the semiconductor layer. These pairs, comprising positively charged holes and negatively charged electrons, travel in opposite directions when subjected to an electric field.

The chip's pixelated elements serve as detectors, capturing and quantifying these charge clouds generated by the interaction of X-ray photons. Each pixel registers the number of charge carriers produced by the incoming photons, and based on this count, discerns the energy levels of absorbed X-ray photons. Through this precise energy measurement, the chip differentiates incoming photons, categorizing them into discrete energy bins—typically five in the case of Medipix 3RX. This distinction enables the chip to provide detailed spectral information, identifying materials and tissues based on their unique energy absorption characteristics. With exceptional energy resolution, the Medipix 3RX chip stands out for its ability to discern X-ray photons based on their energy levels with extraordinary accuracy. Additionally, its pixelated design allows for high spatial resolution, capturing intricate details and structures within the imaged object or specimen. By directly converting X-ray photons into electrical signals without intermediary steps, the chip significantly reduces electronic noise, contributing to clearer and more accurate imaging results (Ballabriga et al., 2013).

The chip's sophisticated capabilities in energy discrimination, high spatial resolution, and noise reduction position it as an indispensable component within photon-counting CT systems. Its precise spectral imaging capabilities significantly enhance diagnostic capabilities in both medical and material science applications, enabling detailed analysis and characterization of diverse materials and tissues.

3.3 QRM Phantom

The QRM phantom is a specialized and standardized phantom used in medical imaging, particularly in quality assurance, calibration, and validation of imaging systems such as computed tomography (CT) scanners. It serves as a controlled test object designed to mimic various tissue properties and structures found in the human body. The QRM phantom is engineered with specific materials and inserts to simulate anatomical features and evaluate imaging performance.

Comprising a robust and reproducible structure, the QRM phantom typically replicates the size and shape of a human body part, often a specific anatomical region or organ system. It's manufactured with materials that imitate human tissues' radiodensity and composition, including various inserts mimicking bones, soft tissues, and sometimes materials like metals or contrast agents to simulate implants or anomalies within the body. The phantom is instrumental in assessing and calibrating CT systems by providing known standards for testing image quality, quantifying accuracy, evaluating resolution, and detecting artifacts. By mimicking human tissues' characteristics, radiologists and technicians can verify and fine-tune imaging parameters, ensuring that the CT scanner produces accurate and reliable images for diagnosis and analysis. Different configurations of the QRM phantom are available, allowing for versatility in the assessment of imaging systems. For instance, there are phantoms designed specifically for bone density measurements, while others focus on assessing soft tissue imaging accuracy. These phantoms come with standardized imaging targets, allowing for comparisons across different CT scanners and imaging protocols.

The QRM phantom serves as a crucial tool in developing and validating novel imaging techniques, quality control procedures, and research studies within the medical imaging field. Its standardized design and known properties make it an essential component for

evaluating and optimizing CT systems to ensure the accuracy and reliability of clinical imaging procedures.



Figure 3.3: Illustrates the QRM Phantom and all the available inserts.

3.4 Data Acquisition

The data collection process involved utilizing ten distinct experimental datasets to establish ground truths and facilitate the training and testing of a Deep Learning (DL) model. This process relied upon the MARS Microlab 5x120, a spectral photon-counting CT developed by MARS Bioimaging Ltd. The scanner incorporates the Medipix 3RX chip, renowned for its capability to segment energy into five distinct bins utilizing charge summing mode.

To acquire the datasets, the MARS Photon-counting CT was employed to scan a QRM Phantom. All scans were performed using 118 kVp tube voltage, 981 circular projections with an exposure time of 160 ms per frame. The tube current was set at 80 μ A to maintain a photon count rate of less than 11 counts/ms to avoid detector saturation and pulse pileup (Aamir et al., 2011). All scans were performed in the charge-summing mode using the default energy thresholds of 40, 50, 60, and 79 keV. The data were reconstructed using the proprietary MARS iterative reconstruction technique in the narrow energy bins, 7-40, 40-50, 50-60, 60-79, and 79-118 KeV. The resulting images had an isotropic voxel size of 0.1 mm and an image matrix of 1300 x 1300.

In this work, six datasets were used for training the MAR algorithm, two datasets for generating simulated images, and the remaining two datasets for validation, see Fig. (3.4). Training datasets include two types of datasets: one dataset comprises variations in the placements of aluminium (99% Al; 20 mm-diameter) and steel (surgical stainless steel; 20 mm-diameter) (shown in Fig. (3.4) (a-d)), while the other dataset consists of varying concentrations of hydroxyapatite (HA) (201.4 and 406.9 mg/cm³) and iodine (9.66, and 14.56 mg/cm³) along with adipose and CT water in the presence of aluminium and steel (Fig. (3.4) (e, f)). The training datasets comprised a scan length of 50 mm: 20 mm containing metal inserts, followed by 10 mm eliminated to prevent the detection of residual artefacts, and 20 mm used as an empty phantom for generating simulated images, as shown in Fig. (3.1). Simulated datasets (Fig. (3.4) (g, h)) were used to extract

metal-specific attenuation profiles of aluminium and steel. After the training of MAR model, we assessed its performance using two validation datasets: the first dataset consisted of aluminium and steel, while the second dataset included varying concentrations of HA and iodine, along with muscle and CT water in the presence of an aluminium insert, as shown in Fig. (3.4) (i, j).

3.5 Artefact Free Simulation

Any supervised deep learning-based MAR technique requires artefact-free images for model training. For this task, simulated images were generated using an automated strategy developed in Python (Python 3.10.12). Datasets for simulation depicted in Fig. (3.4) (g,h) were employed to calculate the mean attenuation and standard deviation values across five energy bins for aluminum and steel, using equations (3.1) and (3.2). The two datasets

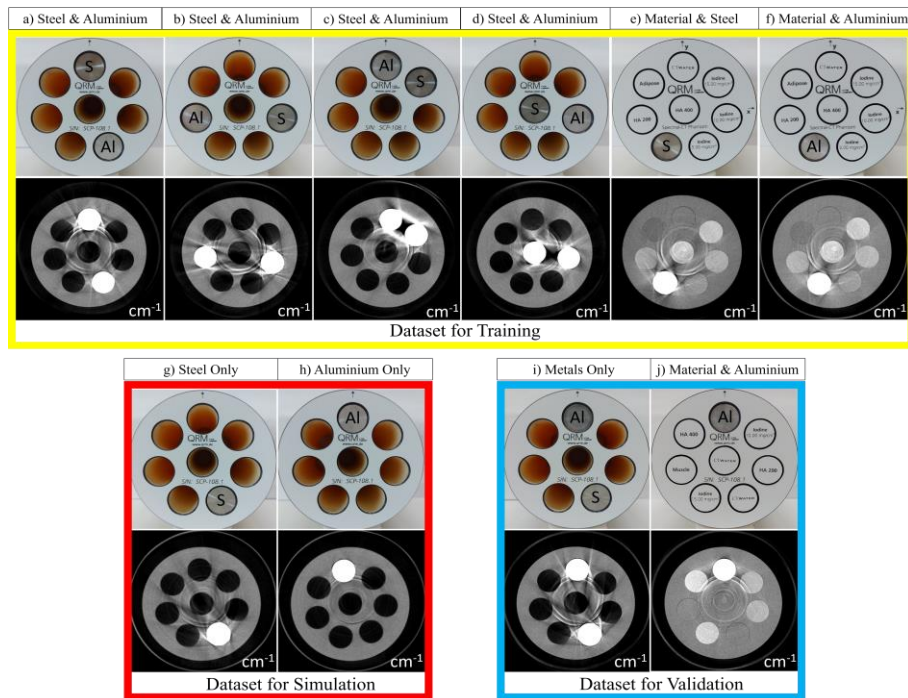


Figure 3.4 Illustration of different datasets used in this study as Phantom image and its CT image across first energy bin (7-40 keV) acquired at 118 kVp and 80 μ A. The training datasets consist of varying placements of steel and aluminium (a-d), while(e,f) contained two concentrations of hydroxyapatite (HA) (201.4 and 406.9 mg/cm^3) and iodine (9.66, and 14.56 mg/cm^3), along with adipose, CT water, in the presence of steel insert (e), and aluminium insert(f). Datasets used for simulation (g,h), consist of only steel, and aluminium inserts, respectively, for extracting material-specific attenuation profiles. Two types of validation datasets (i) a dataset that includes both metal inserts, and (j) a dataset that includes material inserts in the presence of aluminium insert. All energy images are in linear attenuation coefficients (cm^{-1}) in the range of 0 to 0.3 cm^{-1}

consist of individual scans of each metal separately within the phantom, to ensure the extraction of metal-specific profiles without any external factors influencing the results. The values were then superimposed throughout the images of the empty phantoms acquired from the training dataset (Fig. (3.4) (a-f)) in order to obtain artefact-free ground truths for the model training.

$$Mean (\mu) = \frac{1}{N_{mt}} \sum_{i=1}^{N_{mt}} MT_{pix_i} \quad (3.1)$$

$$Standard\ Deviation (\sigma) = \sqrt{\frac{1}{N_{mt} - 1} \sum_{i=1}^{N_{mt}} (MT_{pix_i} - \mu)^2} \quad (3.2)$$

Where:

- μ is the mean value for the metal insert.
- σ is the Standard deviation within the region of the metal insert.
- N_{mt} represents the number of pixels within the circular region for the metal insert.
- MT_{pix_i} represents individual pixel values in the region of the metal insert.

3.6 Deep Learning MAR Algorithm

A SPCCT image array denoted by $I \in \mathbb{R}^{E*L*W}$, where \mathbb{R} is a set of real numbers, E is the number of energy bins, L is the length of the image, and W is the width of the image. A deep learning model is trained to generate an artefact free image array $M \in \mathbb{R}^{E*L*W}$. This process of MAR is expressed as $M = f(I; \theta)$ where, θ contains the learnable parameter of the model.

The proposed MAR algorithm employs a deep learning approach based on RDU-Net performing image-to-image transformation; DenseNet (Huang et al., 2017), ResNet (He et al., 2016), and U-Net (Ronneberger et al., 2015) architectures were combined to create the

RDU-Net architecture. The RDU-Net model was implemented using the PyTorch library, as shown in Fig. (3.5).

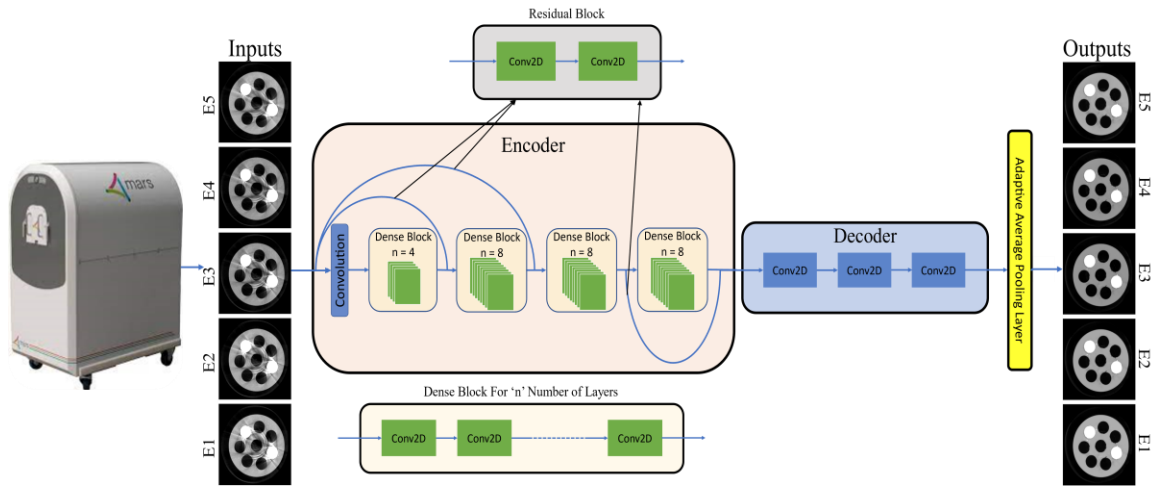


Figure 3.5 Architecture and functioning of the RDU-Net Model For MAR. The RDU-Net Model is an encoder and decoder based architecture. The encoder block consists of four Dense Blocks and three residual connections. The decoder consists of three convolution layers and is followed by an adaptive average pooling layer. The figure depicts how an input image obtained from SPCCT having five energies, containing numerous metal artefacts is corrected using the MAR algorithm to give the artefact free output. E1 (7-40keV), E2 (40-50keV), E3 (50-60keV), E4 (60-79keV) and E5 (79-118keV) represents the five energy bins. Conv2D refer to two-dimensional convolution layers, while 'n' is the number of connected layers in the dense block.

3.6.1 ResNet

ResNet (Residual Network) model was developed to tackle the problem of vanishing gradients in deep neural networks. The vanishing gradient problem arises when gradients decrease exponentially during back-propagation in deep neural networks, impeding the training process and leading to degradation in performance. ResNet addresses this issue by incorporating residual connections, which enable the model to learn residual functions. This innovation allows for the training of significantly deeper networks without a deterioration in performance. Through the integration of residual connections, ResNet

models achieve state-of-the-art performance on various image recognition tasks while being more straightforward to optimize and train in comparison to traditional deep networks.

3.6.2 Densenet

DenseNet, or Densely Connected Convolutional Networks, introduces dense connectivity patterns between layers, where each layer receives feature maps from all preceding layers. This dense interconnection facilitates feature reuse and gradient flow, promoting deeper networks with fewer parameters. This leads to improved feature propagation, ultimately enhancing model performance and training efficiency.

3.6.3 U-net

U-Net is a convolutional neural network architecture designed for biomedical image segmentation tasks. It features a U-shaped architecture with an encoder-decoder structure, where the encoder extracts high-level features and the decoder performs pixel-wise classification. Additionally, U-Net incorporates skip connections between corresponding encoder and decoder layers to preserve spatial information and facilitate precise segmentation.

3.6.4 RDU-Net (Proposed Method)

The RDU-Net architecture features an entry channel of dimensions $5 \times 1300 \times 1300$ and is structured around a U-net type encoder-decoder backbone. The encoder module consists of 4 Dense blocks and 3 residual layers, as shown in Fig. (3.5). The dense block is denoted by $D = X_0 \oplus f_1(X_0; \theta_0) \oplus \dots \oplus f_n(X_n; \theta_n)$, where ‘ X ’ represents the feature map, ‘ \oplus ’ represents the concatenation operation, ‘ f ’ represents the convolution function, and ‘ n ’ represents the number of layers in the dense block. The dense block connects each layer to every other layer in a feed-forward fashion by concatenating features after every layer. This dense connectivity facilitates feature reuse, encourages feature propagation, and enhances gradient flow throughout the network, resulting in more efficient feature extraction. The first dense layer consists of 4 connected layers while the remaining three consists of 8 connected layers each. The residual layers include two 2D convolution layers and are

combined with the dense blocks within the encoder. The initial two residual layers establish connections between the input and the first two dense layers, thereby mitigating the risk of gradient vanishing and preserving features from the input. The last residual layer interconnects the third and fourth dense layers, ensuring stability in gradient propagation. Subsequently, the decoder comprises of three 2D convolution layers to reconstruct the encoded image back to its original input format. An adaptive average pooling layer is applied following the encoder-decoder sequence to adjust the output dimensions to match those of the input. For model training, we employed the L1 Loss Function along with the Adam optimizer, utilizing a learning rate of 0.001. Various loss functions, including MSE and BCE loss, were tested, but L1 loss gave more distinct boundaries. The utilization of the adam optimizer contributed to faster convergence of gradients, leading to a quicker and more accurate reduction in loss. This resulted in a decreased number of epochs required for convergence.

3.7 Evaluation Strategy

Evaluation of the RDU-Net-driven MAR algorithm comprises two distinct phases: validation using a dataset containing only metal inserts, and validation using a dataset encompassing both materials and metal inserts. The initial validation of the first dataset consists of analyzing images across five discrete energy bins, referred to as "Energy Analysis." The second evaluation of the second dataset involves the utilization of density images, identified as "Material Analysis."

3.7.1 Energy Analysis

Three major techniques were employed in order to conduct a thorough Energy Analysis of the obtained results. The spectral response of the first validation dataset (Fig. (3.4) (i)) was analysed using line profiles (with a length of 30 mm) through the centre of the inserts. These lines were consistently positioned across all five energy bin images, see Fig. (4.2) (a, b). Furthermore, plotting the histogram for the six Region of Interests (ROIs), as indicated in Fig. (4.3) (a), cumulatively across all energy bins allowed us to study the difference in the distribution of the linear attenuation values in input, simulated, and output images. For the statistical assessment of these energy images, Signal-to-noise ratio (SNR),

root mean squared error (RMSE), and structural similarity index measure (SSIM) were calculated.

The SNR and the RMSE were calculated using equations (3.3) and (3.4), respectively, within the same six ROIs. SNR represents the ratio between the mean attenuation and the standard deviation values inside the ROI. A higher SNR indicates that the signal is more prominent relative to the noise, which generally corresponds to a clearer and more accurate representation of the imaged structures.

Signal-to-Noise Ratio (SNR):

SNR measures the ratio between the power of a signal and the power of corrupting noise that affects the quality of its representation. For images, it's used to quantify the quality of output image to the original image.

$$SNR = \left(\frac{\mu}{\sigma}\right) \quad (3.3)$$

Where:

- μ is the mean attenuation value of the ROI.
- σ is the standard deviation within the ROI.

Root Mean Squared Error (RMSE):

RMSE measures the average of the squares of the errors between corresponding values of the original and reconstructed images. It's a standard measure of the differences between values predicted by a model or an estimator and the values observed.

$$RMSE = \sqrt{\frac{1}{n} \sum_{i=1}^n (x_i - y_i)^2} \quad (3.4)$$

Where:

- x_i and y_i are the corresponding pixel values of the original and predicted images.
- n is the total number of pixels in the image.

The SSIM was employed using equation (3.5) to quantitatively evaluate the similarity across the entire scanned phantom, as shown in Fig. (4.4) (d).

Structural Similarity Index (SSIM):

SSIM measures the similarity between two images. It considers luminance, contrast, and structural similarity between two images to provide a value between -1 and 1, where 1 indicates perfect similarity.

$$SSIM(x, y) = \frac{(2\mu_x\mu_y + C_1)(2\sigma_{xy} + C_2)}{(\mu_x^2 + \mu_y^2 + C_1)(\sigma_x^2 + \sigma_y^2 + C_2)} \quad (3.5)$$

Where:

- x and y are the two compared images.
- μ_x and μ_y are the means of x and y .
- σ_x^2 and σ_y^2 are the variances of x and y .
- σ_{xy} is the covariance of x and y .
- C_1 and C_2 are constants to stabilize the division with weak denominator.

3.7.2 Material Analysis

The Material Analysis was conducted using the validation dataset that contain materials and metal inserts (as shown in Fig. (3.4) (j)) to evaluate the effect of MAR algorithm on material identification and quantification obtained through MD on CT images. All energy images were converted to material density images using vendor-provided MARS-FASTMD v1.4 software. The software employs the basis vectors and the linear least

squares estimation to predict the material combinations and concentrations from the attenuation profiles (Aamir Younis et al., 2018). Additional details on Mars MD are found in (Bateman et al., 2018). The MD algorithm was utilized to decompose input and output images, both with and without MAR algorithm, into HA and I. The QRM phantom contained two concentrations of HA (201.4 and 406.9 mg/cm³) and I (9.66 and 14.56 mg/cm³), along with water, and muscle. Material decomposition were quantitatively assessed using Python 3.10.12. The sensitivity was determined by comparing voxel counts in a ROI for the target material in density images against ground truth energy images. The specificity was evaluated for the entire density image ROI against the target material ROI. The comprehensive quantitative assessment encompassed additional metrics, including accuracy, positive predicted value (PPV), and negative predicted value (NPV).

CHAPTER 4: RESULTS

4.1 Energy Analysis:

In this section, we present the results of the Energy Analysis using our proposed machine learning model. Fig. (4.1) shows the validation dataset we used for this analysis. The input images included various prominent artefacts including streaking, increased noise, as well as deep ring artefacts that were significantly enhanced in the presence of metals. The qualitative evaluation of the output images, after the application of MAR, shows a considerable decrease in these artefacts. Nevertheless, a subtle spatial distortion was observed in the output images, particularly in regions impacted by ring artefacts and in close proximity to metals. However, the extent of this distortion progressively diminishes from Fig. (4.1) (c₁) to (c₅) as the energy level increases.

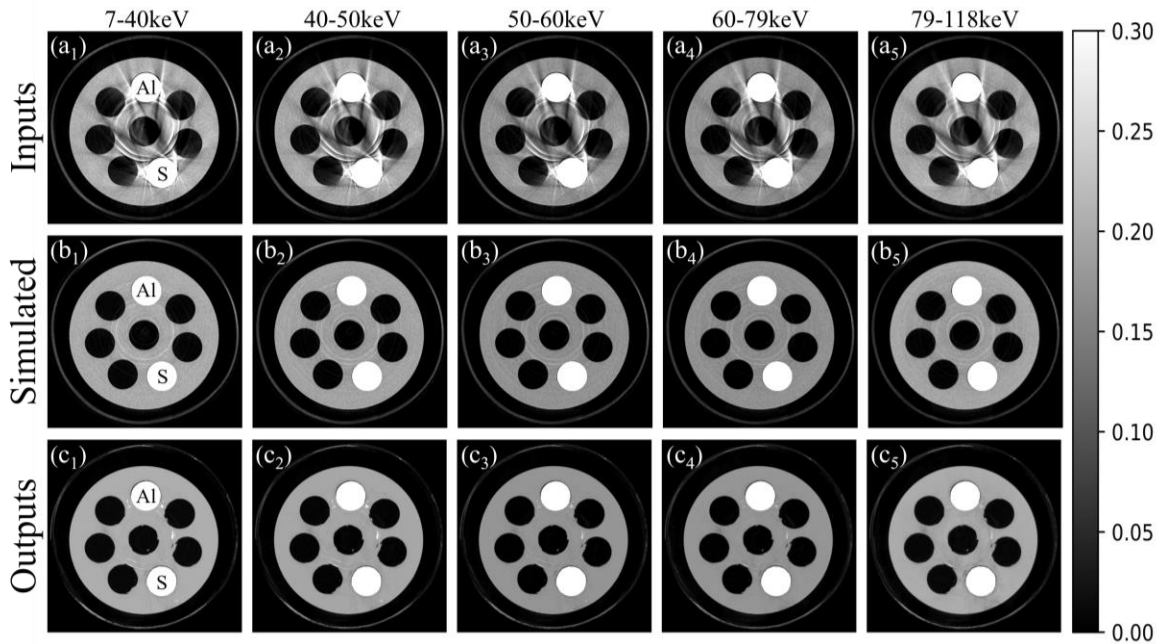


Figure 4.1 The validation dataset contains input images (a), simulated images (b), and output images(c) in the presence of steel (S) and aluminium (Al). Input images were acquired at 118kVp and 80 μ A across five energy bins (a). The simulated images were created using mathematical simulation in order to generate artefact-free reference images (b). The output images (c) are the input images (a) corrected

using the proposed RDU-Net model. The grayscale bar represents the linear attenuation coefficient range from 0 to 0.3 cm^{-1} .

Fig. (4.2) illustrates the line profiles of the linear attenuation coefficient across both steel and Aluminium metal inserts. The line profiles show gross overestimation of linear attenuation coefficients at the edges of the metal inserts, which can be observed as two steep peaks seen in the line profiles of Fig. (4.2) (b) for aluminium and Fig. (4.2) (f) for steel. Furthermore, it is noticeable that this overestimation is particularly pronounced in steel, which consistently displays elevated levels of noise even at higher energies. In contrast, for aluminium, the height of the peaks diminishes, indicating a reduction in artefacts and noise compared to steel. Remarkably, in Fig. (4.2) (d) and Fig. (4.2) (h), it is evident how the utilization of the RDU-Net model eliminates the metal artefact, reduces the noise and produces sharper edges.

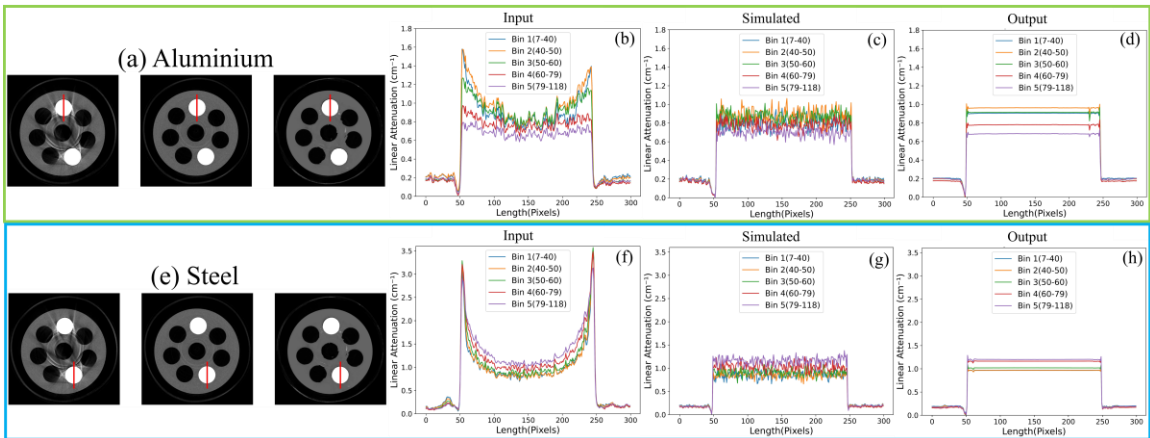


Figure 4.2 Line profiles 30 mm in length (shown in red color), passing through the center of both the aluminium (a) and the steel (e) inserts showing the linear attenuation values in the input, simulated, and output images in the validation datasets shown in Fig. (4.1)

Fig. (4.3) demonstrates the spread of pixel values along the phantom body. The histogram analysis reveals consistently narrower spreads in the output images, indicating lower noise effects compared to the input images. Fig. (4.3) (g) illustrates the percentage differences between the mean values of the pixel values across the five energy bins.

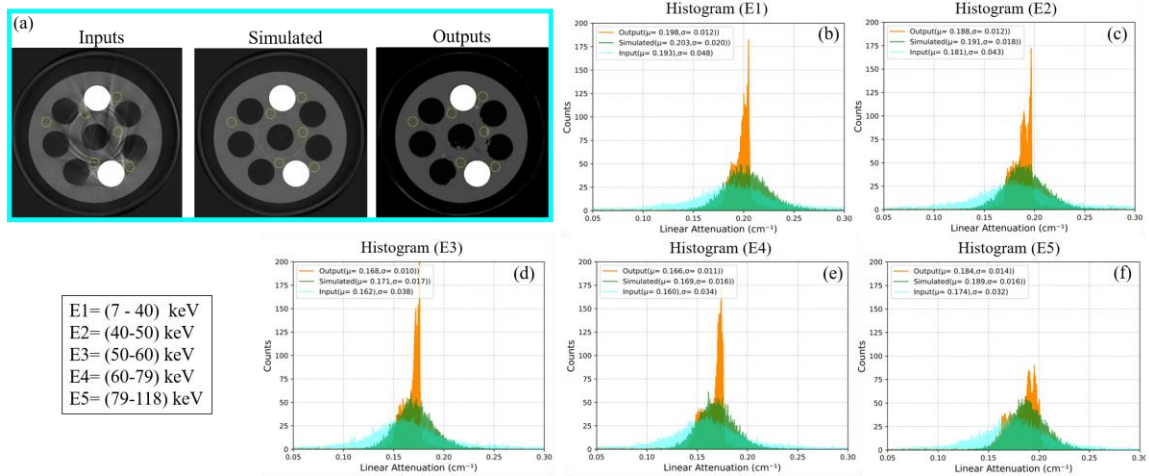


Figure 4.3 (a) Six ROIs, indicated by the yellow circles, were used to plot the histograms of pixel values in different regions of the phantom. (b), (c), (d), (e) and (f) are the histogram plots for the input, simulated and output images in the five respective energy bins. (g) The percentage difference between the mean values of the input and output images compared to the simulated images.

Fig. (4.4) shows the graphical representation of the evaluation metrics. Fig. (4.4) (a) shows the ROIs that were selected in order to calculate SNR and RMSE results. SNR results, calculated for the input and output images across the five energy bins, are shown in Fig. (4.4) (b). Additionally, the comparison of the RMSE values, calculated between input and simulated images, and between output and simulated images, are shown in Fig. (4.4) (c). Moreover, the comparison of the SSIM values, calculated between the input and the simulated images, and between the input and the output images, are shown in Fig. (4.4) (d).

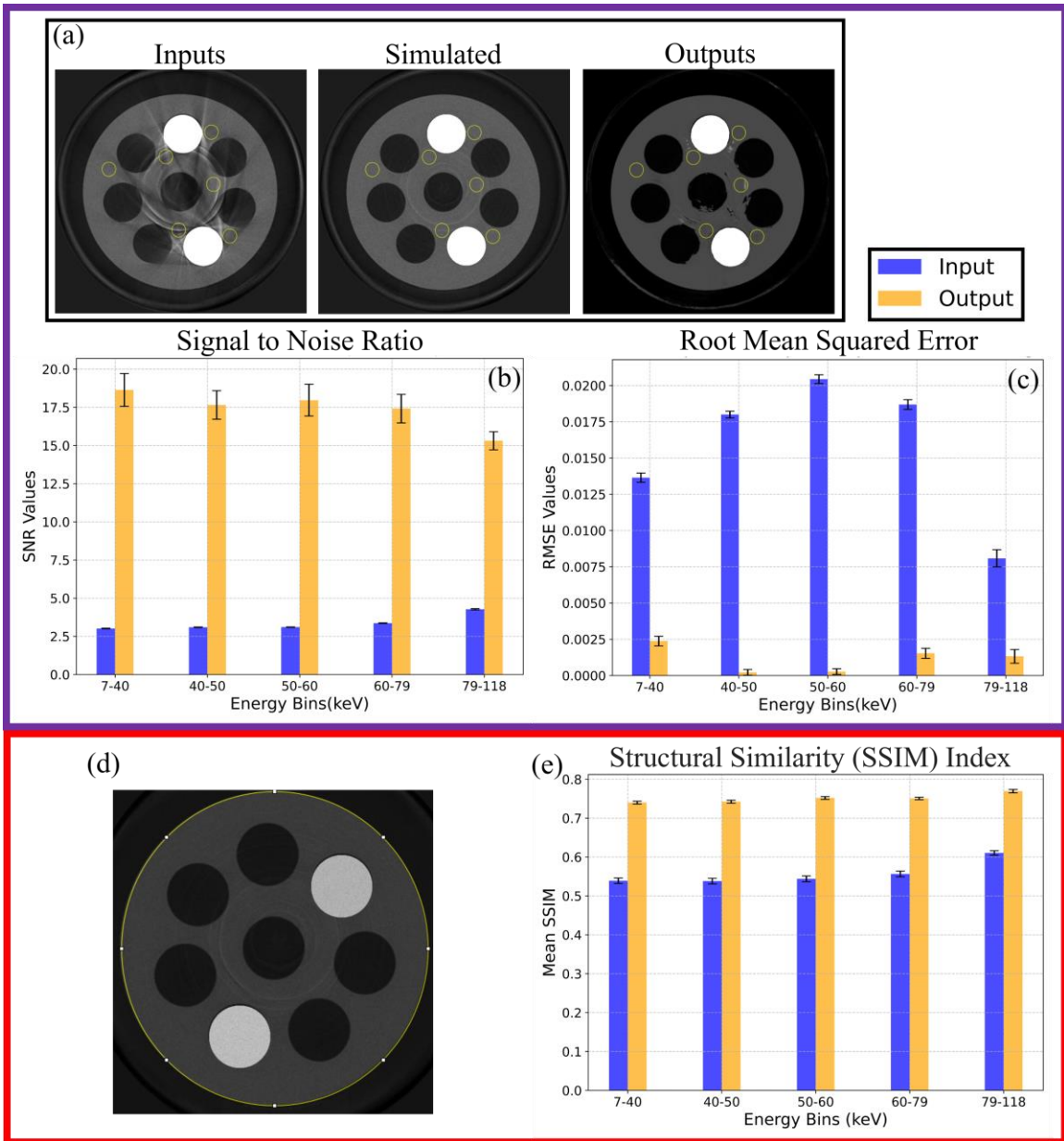


Figure 4.4: The Evaluation metrics for the MAR algorithm. (a) The ROIs used for the calculation of SNR and RMSE calculations. (b) Graph for input and output SNR and (c) RMSE values of Input to Output calculated with respect to the simulated images. (d) The ROI for SSIM calculation and (e) SSIM of the input and output images with respect to simulated images.

4.2 Material Analysis

In this section, we present the results of the Material Analysis using our proposed machine learning model. Fig. (4.5) (b) and (c) show the phantom material density images of both HA and I without MAR. On the other hand, Fig. (4.5) (f) and (g) show the phantom material density images of HA and I after the application of the proposed MAR algorithm. Following the implementation of MAR algorithm, a significant improvement in the accuracy of the MD was observed. Artefacts misclassified as HA and I were properly identified and corrected after the application of MAR. In Fig. (4.5) (d) and (h), the voxel-wise distribution of HA and I is depicted based on known concentrations, with and without MAR algorithm, utilizing the box and whiskers plot. The smaller size of the boxes and whiskers for both materials highlight a notable reduction in material density distributions when the MAR algorithm is applied.

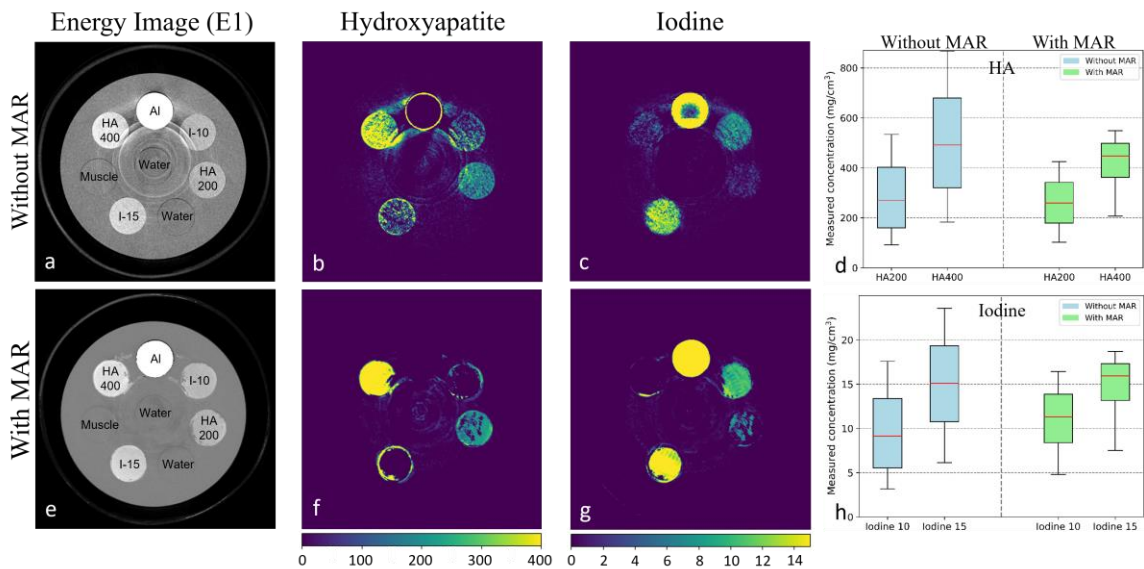


Figure 4.5 The results of the Material Analysis after using MAR algorithm. (a) shows the first energy bin image obtained from the SPCCT containing aluminium and material inserts. (b) and (c) show the material density images of hydroxyapatite (HA) and iodine (I) obtained from the image shown in (a). (d) Shows the box whiskers plot for HA with and without MAR. (e) Shows the output obtained after the application of MAR algorithm on (a). (f) and (g) show the material density images of HA and I obtained from the scan shown in (e), after the application of

MAR algorithm. (h) Shows the box whiskers plot for Iodine with and without MAR. The materials labels are 'Al' for aluminium, HA200 and 400 are for hydroxyapatite concentrations of 201.4 and 406.9 mg/cm³ respectively. I-10 and I-15 refers to iodine concentrations of 9.66, and 14.56 mg/cm³ respectively.

Performance parameters including, sensitivity, specificity, accuracy, Negative Predictive values (NPV), and Positive Predictive Value (PPV) for the material density images of I and HA, with and without MAR are shown in Table 4.1.

Table 4.1 Material Identification (sensitivity, specificity, Accuracy, NPV, and PPV) and quantification (RMSE) analysis for material decomposition of hydroxyapatite (HA) and Iodine(I) without and with metal artefact reduction (MAR), in the presence of aluminium insert.

| Material (mg/cm ³) | Material Identification | | | | | Material Quantification |
|-----------------------------------|-------------------------|--------------------|-----------------|---------------|------------------|-------------------------------|
| | Sensitivity (%) | Specificity (%) | Accuracy (%) | Recall (%) | Precision (%) | RMSE (mg/cm ³) |
| HA | 74 | 90 | 8 | 91 | 73 | 0.937 |
| HA with MAR | 85 | 94 | 91 | 91 | 91 | 0.117 |
| Iodine | 72 | 9 | 84 | 88 | 74 | 0.049 |
| Iodine with MAR | 90 | 94 | 93 | 96 | 86 | 0.003 |

DISCUSSION

The RDU-Net exhibits good performance across all evaluated metrics, as detailed in the study. It effectively mitigates artefacts induced by metallic objects while accurately preserving multi-energy attenuation characteristics. This capability ensures the retention of spectral data integrity and the post-artefact correction. Moreover, the algorithm underwent elaborate energy and material analyses to quantitatively assess its effectiveness. As illustrated in Fig. (4.1) (a), input images showed significant streaking and overestimation of the attenuation coefficient in all energy bins. Moreover, an increase in the depth of ring artefacts was also observed, which is more prominent in the proximity of the metal inserts. Fig. (4.1) (c) shows the corrected images obtained from the proposed MAR algorithm. The visual analysis of the two images shows a significant reduction in metal artefacts, ring artefacts, and noise levels.

Fig. (4.2) illustrates the line profiles of aluminium and steel. In Fig. (4.2) (b) we can observe that aluminium has considerably less NLPV and cupping artefacts in the higher energy bins as the peaks at the edges of the aluminium profile nearly vanish in these bins. Steel however, has much more prominent artefacts which did not insignificantly decrease at higher energies, as can be seen in Fig. (4.2) (f). Additionally, it was observed that the mean linear attenuation coefficient of the region containing steel increased with the increasing energy level, primarily due to the cupping artefact. The pronounced artefacts observed in steel arise mainly from its substantially higher density, 7.98 g/cm^3 , in contrast to the comparatively lower density of aluminium, 2.71 g/cm^3 . Nevertheless, the application of the MAR algorithm effectively eliminates most of artefacts including NLPV, cupping artefacts, as well as noise for both metals, as shown in Fig. (4.2) (d, h).

Fig. (4.3) illustrates this observation, indicating that although the mean linear attenuation values of the output images closely matches those of the simulated images, there is a consistent reduction in the spread or width of the histogram. This indicates that the algorithm corrects the images without significant effecting to the attenuation profiles, thus maintaining the integrity of the extracted data. In Fig. (4.4) (b), we observe a significant improvement of SNR in the output images, compared to the input images, indicating a

substantial reduction in the noise following the application of MAR algorithm. Moreover, Fig. (4.4) (c) demonstrates that the RMSE of the output images is notably lower than that of the input images, indicating a closer resemblance to the artefact-free simulated images. Additionally, Fig. (4.4) (e) illustrates the higher structural similarity between the output and the simulated images, which shows that our algorithm maintains the spatial and attenuation profile integrity while correcting the noise and artefacts from the scan images.

Furthermore, we conducted Material Analysis to assess the impact of MAR algorithm on MD. Fig. (4.5) (b) and (c) illustrate substantial loss of material information and misidentification that occurs as a result of streaking and noise. However, after applying the MAR algorithm, we observe a significant improvement in the density images of both HA and I, Fig. (4.5) (f) and (g), show more accurate material identification and decomposition. The box plot graphs for HA, shown in Fig. (4.5) (d) and I, shown in Fig. (4.5) (h), similarly demonstrate improvement as the variations in calculated densities for both materials decrease.

This is evident from the reduction in the size of the box and whiskers in the plots after implementing MAR algorithm. Additionally, the quantification becomes more accurate, with the median positioned closer to the actual values in both plots following the application of MAR. Furthermore, Table (4.1) provides statistical quantification of these enhancements, revealing a significant improvement in all evaluation metrics following the implementation of the MAR algorithm.

CONCLUSION & FUTURE PROSPECTS

The proposed RDU-Net has demonstrated promising results, exhibiting improvements in artefact-affected images across all evaluation metrics. This advancement represents a significant step towards the development of a commercially viable MAR algorithm for Single Photon-counting Computed Tomography (SPCCT). The algorithm not only effectively eliminates artefacts but also retains comprehensive spectral information from the scans. This capability holds immense potential for facilitating advanced analyses, as evident from the results of MD presented in the paper. However, the MAR algorithm needs to be trained and tested on more versatile biological datasets in order to validate it for clinical application.

Looking ahead, the future prospects of the RDU-Net algorithm are promising. With further refinement and optimization, this algorithm holds much potential. Its ability to accurately correct artefact-affected images while preserving spectral information opens doors to a wide range of applications. For instance, in oncology, the enhanced imaging provided by RDU-Net could lead to more accurate tumor detection and characterization, ultimately improving treatment planning and patient outcomes. Additionally, in cardiology, the algorithm's ability to mitigate artefacts in cardiac CT scans could improve the diagnosis of cardiovascular diseases and enhance preoperative planning for cardiac surgeries. Moreover, the algorithm's adaptability and robustness make it suitable for integration into existing CT systems, offering a seamless solution for clinicians and radiologists. As the field of medical imaging continues to evolve, the RDU-Net algorithm can make significant positive changes, paving the way for more precise diagnoses, personalized treatments, and improved patient care.

REFERENCES

- Aamir, R., Lansley, S. P., Zainon, R., Fiederle, M., Fauler, A., Greiffenberg, D., Butler, P. H., & Butler, A. P. H. (2011). Pixel sensitivity variations in a CdTe-Medipix2 detector using poly-energetic x-rays. *Journal of Instrumentation*, 6(01), C01059.
- Aamir Younis, R., Mahdieh, M., Christopher, J. B., Niels de, R., Benjamin, S., Nanette, S., Tim, B. F. W., Anthony, P. H. B., & Nigel, G. A. (2018). Measuring identification and quantification errors in spectral CT material decomposition. *Applied Sciences (Switzerland)*, 8. <https://doi.org/10.3390/app8030467>
- Arabi, H., & Zaidi, H. (2021). Deep learning--based metal artefact reduction in PET/CT imaging. *European radiology*, 31, 6384--6396.
- Ballabriga, R., Alozy, J., Bandi, F. N., Campbell, M., Egidos, N., Fernandez-Tenllado, J. M., Heijne, E. H. M., Kremastiotis, I., Llopart, X., Madsen, B. J., Pennicard, D., Sriskaran, V., & Tlustos, L. (2021). Photon-counting Detectors for X-Ray Imaging With Emphasis on CT. *IEEE Transactions on Radiation and Plasma Medical Sciences*, 5(4), 422-440. <https://doi.org/10.1109/TRPMS.2020.3002949>
- Ballabriga, R., Alozy, J., Blaj, G., Campbell, M., Fiederle, M., Frojdh, E., Heijne, E. H. M., Llopart, X., Pichotka, M., Procz, S., & et al. (2013). The Medipix3RX: a high resolution, zero dead-time pixel detector readout chip allowing spectroscopic imaging. *Journal of Instrumentation*, 8(02), C02016.
- Ballhausen, H., Reiner, M., Ganswindt, U., Belka, C., & Söhn, M. (2014). Post-processing sets of tilted CT volumes as a method for metal artifact reduction. *Radiation Oncology*, 9, 1-10.
- Bateman, C. J., Knight, D., Brandwacht, B., Mahon, J. M., Healy, J., Panta, R., Aamir, R., Rajendran, K., Moghiseh, M., Ramyar, M., Rundle, D., Bennett, J., Ruiter, N. D., Smithies, D., Bell, S. T., Doesburg, R., Chernoglazov, A., Mandalika, V. B. H., Walsh, M., . . . Butler, P. H. (2018). MARS-MD: Rejection based image

domain material decomposition. *Journal of Instrumentation*, 13.
<https://doi.org/10.1088/1748-0221/13/05/P05020>

- Battista, J. J., Rider, W. D., & Van Dyk, J. (1980). Computed tomography for radiotherapy planning. *International Journal of Radiation Oncology* Biology* Physics*, 6(1), 99--107.
- Boas, F. E., Fleischmann, D., & et al. (2012). CT artifacts: causes and reduction techniques. *Imaging Med*, 4(2), 229--240.
- Busi, M., Kehl, C., Frisvad, J. R., & Olsen, U. L. (2022). Metal artifact reduction in spectral X-ray CT using spectral deep learning. *Journal of Imaging*, 8(3), 77.
- Coupal, T. M., Mallinson, P. I., McLaughlin, P., Nicolaou, S., Munk, P. L., & Ouellette, H. (2014). Peering through the glare: using dual-energy CT to overcome the problem of metal artefacts in bone radiology. *Skeletal radiology*, 43(5), 567--575.
- Danielsson, M., Persson, M., & Sjölin, M. (2021). Photon-counting x-ray detectors for CT. *Physics in Medicine & Biology*, 66(3), 03TR01.
- De Man, B., Nuyts, J., Dupont, P., Marchal, G., & Suetens, P. (1998). *Metal streak artifacts in X-ray computed tomography: a simulation study*
- DenOtter, T. D., & Schubert, J. (2023). *Hounsfield Unit*. StatPearls Publishing, Treasure Island (FL). <http://europepmc.org/abstract/MED/31613501>
- Duan, X., Zhang, L., Xiao, Y., Cheng, J., Chen, Z., & Xing, Y. (2008). *Metal artifact reduction in CT images by sinogram TV inpainting*
- Esses, D., Birnbaum, A., Bijur, P., Shah, S., Gleyzer, A., & Gallagher, E. J. (2004). Ability of CT to alter decision making in elderly patients with acute abdominal pain. *The American journal of emergency medicine*, 22(4), 270--272.

- Flohr, T., Ulzheimer, S., Petersilka, M., & Schmidt, B. (2020). Basic principles and clinical potential of photon-counting detector CT. *Chinese Journal of Academic Radiology*, 3, 19--34.
- Gjesteby, L., De Man, B., Jin, Y., Paganetti, H., Verburg, J., Giantsoudi, D., & Wang, G. (2016). Metal artifact reduction in CT: where are we after four decades? *Ieee Access*, 4, 5826--5849.
- Glover, G. H., & Pelc, N. J. (1980). Nonlinear partial volume artifacts in x-ray computed tomography. *Medical Physics*, 7(3), 238--248.
- Gücük, A., & Üyetürk, U. (2014). Usefulness of hounsfield unit and density in the assessment and treatment of urinary stones. *World journal of nephrology*, 3(4), 282.
- He, K., Zhang, X., Ren, S., & Sun, J. (2016). *Deep residual learning for image recognition*
- Hegazy, M. A. A., Cho, M. H., Cho, M. H., & Lee, S. Y. (2019). U-net based metal segmentation on projection domain for metal artifact reduction in dental CT. *Biomedical engineering letters*, 9(3), 375--385.
- Hsieh, J. (2009). Computed tomography: principles, design, artifacts, and recent advances.
- Huang, G., Liu, Z., Van Der Maaten, L., & Weinberger, K. Q. (2017). *Densely connected convolutional networks*
- Huang, X., Wang, J., Tang, F., Zhong, T., & Zhang, Y. (2018). Metal artifact reduction on cervical CT images by deep residual learning. *Biomedical engineering online*, 17, 1-15.
- Hunter, A. K., & McDavid, W. D. (2012). Characterization and correction of cupping effect artefacts in cone beam CT. *Dentomaxillofacial Radiology*, 41(3), 217--223.

- Ibrahim, Y. O., Maalej, N., Pirzada, B. M., Raja, A. Y., Anjum, D. H., Jan, N., Behouch, A., & Qurashi, A. U. H. (2024). Gold nanoparticles spectral CT imaging and limit of detectability in a new materials contrast-detail phantom. *Physica Medica*, *120*, 103326.
- Kim, C., Pua, R., Lee, C. H., Choi, D. i., Cho, B., Lee, S. w., Cho, S., & Kwak, J. (2019). An additional tilted-scan-based CT metal-artifact-reduction method for radiation therapy planning. *Journal of Applied Clinical Medical Physics*, *20*(1), 237-249.
- Koonsanit, K., Chanwimaluang, T., Gansawat, D., Sotthivirat, S., Narkbuakaew, W., Areeprayolkij, W., Yampri, P., & Sinthupinyo, W. (2009). Metal Artifact Removal on Dental CT Scanned Images by Using Multi-Layer Entropic Thresholding and Label Filtering Techniques for 3-D Visualization of CT Images. 13th International Conference on Biomedical Engineering: ICBME 2008 3–6 December 2008 Singapore,
- Lee, C.-L., Park, J., Nam, S., Choi, J., Choi, Y., Lee, S., Lee, K.-Y., & Cho, M. (2021). Metal artifact reduction and tumor detection using photon-counting multi-energy computed tomography. *Plos one*, *16*(3), e0247355.
- Leng, S., Bruesewitz, M., Tao, S., Rajendran, K., Halaweish, A. F., Campeau, N. G., Fletcher, J. G., & McCollough, C. H. (2019). Photon-counting detector CT: system design and clinical applications of an emerging technology. *Radiographics*, *39*(3), 729--743.
- Liao, H., Lin, W.-A., Zhou, S. K., & Luo, J. (2019). ADN: artifact disentanglement network for unsupervised metal artifact reduction. *IEEE Transactions on Medical Imaging*, *39*(3), 634--643.
- Lin, W.-A., Liao, H., Peng, C., Sun, X., Zhang, J., Luo, J., Chellappa, R., & Zhou, S. K. (2019). *Dudonet: Dual domain network for ct metal artifact reduction*

- Mettler Jr, F. A., Thomadsen, B. R., Bhargavan, M., Gilley, D. B., Gray, J. E., Lipoti, J. A., McCrohan, J., Yoshizumi, T. T., & Mahesh, M. (2008). Medical radiation exposure in the US in 2006: preliminary results. *Health physics*, 95(5), 502--507.
- Meyer, E., Maaß, C., Baer, M., Raupach, R., Schmidt, B., & Kachelrieß, M. (2010). Empirical scatter correction (ESC): A new CT scatter correction method and its application to metal artifact reduction. IEEE Nuclear Science Symposium & Medical Imaging Conference,
- Moghiseh, M., Clark, J. A., Amma, M. R., Chapagain, K. M., Dixit, D., Lowe, C., Matanaghi, A., Searle, E., Sayous, Y., & Kumar, D. (2023). MARS for molecular imaging and preclinical studies. In *Photon-counting Computed Tomography: Clinical Applications, Image Reconstruction and Material Discrimination* (pp. 63-92). Springer.
- Mouton, A., Megherbi, N., Flitton, G. T., Bizot, S., & Breckon, T. P. (2012). A novel intensity limiting approach to metal artefact reduction in 3D CT baggage imagery. 2012 19th IEEE International Conference on Image Processing,
- Nicol, E. D., Norgaard, B. L., Blanke, P., Ahmadi, A., Weir-McCall, J., Horvat, P. M., Han, K., Bax, J. J., & Leipsic, J. (2019). The future of cardiovascular computed tomography: advanced analytics and clinical insights. *Cardiovascular Imaging*, 12(6), 1058--1072.
- Prell, D., Kyriakou, Y., Beister, M., & Kalender, W. A. (2009). A novel forward projection-based metal artifact reduction method for flat-detector computed tomography. *Physics in Medicine & Biology*, 54(21), 6575.
- Puvasunthararajah, S., Fontanarosa, D., Wille, M.-L., & Camps, S. M. (2021). The application of metal artifact reduction methods on computed tomography scans for radiotherapy applications: A literature review. *Journal of Applied Clinical Medical Physics*, 22(6), 198--223.

- Richtsmeier, D., Rodesch, P.-A., Iniewski, K., Siu, W., & Bazalova-Carter, M. (2023). The feasibility of accurate stent visualization with photon-counting detector CT and K-edge imaging. *IEEE Transactions on Radiation and Plasma Medical Sciences*.
- Rodríguez-Gallo, Y., Orozco-Morales, R., & Pérez-Díaz, M. (2019). Metal artifact reduction by morphological image filtering for computed tomography. World Congress on Medical Physics and Biomedical Engineering 2018: June 3-8, 2018, Prague, Czech Republic (Vol. 1),
- Ronneberger, O., Fischer, P., & Brox, T. (2015). *U-net: Convolutional networks for biomedical image segmentation*
- Schmidt, T. G., Sammut, B. A., Barber, R. F., Pan, X., & Sidky, E. Y. (2022). Addressing CT metal artifacts using photon-counting detectors and one-step spectral CT image reconstruction. *Medical Physics*, 49(5), 3021-3040.
- Sripes, P. G., & Yaparalvi, R. (2012). *Technical aspects of positron emission tomography/computed tomography in radiotherapy treatment planning*
- Skornitzke, S., Mergen, V., Biederer, J., Alkadhi, H., Do, T. D., Stiller, W., Frauenfelder, T., Kauczor, H.-U., & Euler, A. (2023). Metal artifact reduction in photon-counting detector CT: quantitative evaluation of artifact reduction techniques. *Investigative Radiology*, 10--1097.
- Vellarackal, A. J., & Kaim, A. H. (2021). Metal artefact reduction of different alloys with dual energy computed tomography (DECT). *Scientific Reports*, 11(1), 2211.
- Wang, G., Snyder, D. L., O'Sullivan, J. A., & Vannier, M. W. (1996). Iterative deblurring for CT metal artifact reduction. *IEEE Transactions on Medical Imaging*, 15(5), 657--664.
- Wijesekera, N. T., Duncan, M. K., & Padley, S. P. G. (2010). X-ray computed tomography of the heart. *British medical bulletin*, 93(1), 49--67.

- Willemink, M. J., Persson, M., Pourmorteza, A., Pelc, N. J., & Fleischmann, D. (2018). Photon-counting CT: technical principles and clinical prospects. *Radiology*, 289(2), 293--312.
- Willi, A. K. (2006). X-ray computed tomography. *Physics in Medicine & Biology*, 51(13), R29. <https://doi.org/10.1088/0031-9155/51/13/R03>
- Withers, P. J., Bouman, C., Carmignato, S., Cnudde, V., Grimaldi, D., Hagen, C. K., Maire, E., Manley, M., Du Plessis, A., & Stock, S. R. (2021). X-ray computed tomography. *Nature Reviews Methods Primers*, 1(1), 18.
- Wu, Y., Ye, Z., Chen, J., Deng, L., & Song, B. (2023). Photon-counting CT: technical principles, clinical applications, and future prospects. *Academic radiology*.
- Yu, L., Zhang, Z., Li, X., Ren, H., Zhao, W., & Xing, L. (2021). Metal artifact reduction in 2D CT images with self-supervised cross-domain learning. *Physics in Medicine & Biology*, 66(17), 175003.
- Zhang, X., Wang, J., & Xing, L. (2011). Metal artifact reduction in x-ray computed tomography (CT) by constrained optimization. *Medical Physics*, 38(2), 701-711.
- Zhang, Y., & Yu, H. (2018). Convolutional neural network based metal artifact reduction in x-ray computed tomography. *IEEE Transactions on Medical Imaging*, 37(6), 1370--1381.
- Zheng, H., Yang, M., Jia, Y., Zhang, L., Sun, X., Zhang, Y., Nie, Z., Wu, H., Zhang, X., & Lei, Z. (2022). A novel subtraction method to reduce metal artifacts of cerebral aneurysm embolism coils. *Clinical Neuroradiology*, 32(3), 687-694.